Some atmospheric processes governing the large-scale tropical circulation in idealized aqua-planet simulations

Guillaume Gastineau *

Laboratoire d'Océanographie et du Climat: Expérimentation et Approches Numériques (LOCEAN),

IPSL/CNRS, Université Pierre et Marie Curie-Paris 6, Paris, France

Laurent Li

Laboratoire de Météorologie Dynamique, Université Pierre et Marie Curie-Paris6 / CNRS, Paris, France

Hervé Le Treut

Institut Pierre Simon Laplace / CNRS, Paris, France

* *Corresponding author address:* Guillaume Gastineau, LOCEAN/IPSL, Paris, France

E-mail: Guillaume.Gastineau@locean-ipsl.upmc.fr

ABSTRACT

The large-scale tropical atmospheric circulation is analyzed in idealized aqua-planet simulations using an atmospheric general circulation model. Idealized Sea Surface Temperatures (SSTs) are used as lower-boundary conditions to provoke modifications of the atmospheric general circulation. Results show that (1) an increase in the meridional SST gradients of the tropical region drastically strengthens the Hadley circulation intensity; (2) the presence of equatorial zonal SST anomalies weakens the Hadley cells and reinforces the Walker circulation, (3) a uniform SST warming causes small and non-systematic changes of the Hadley and Walker circulations. In all simulations, the jet streams strengthen and move equatorward as the Hadley cells strengthen and become narrower.

Some relevant mechanisms are then proposed to interpret the large range of behaviors obtained from the simulations. Firstly, the zonal momentum transport by transient and stationary eddies is shown to modulate the eddy-driven jets, which causes the poleward displacements of the jet streams. Secondly, it is found that the Hadley circulation adjusts to the changes of the poleward moist static energy flux and gross moist static stability, associated with the geographical distribution of convection and midlatitude eddies. The Walker circulation intensity corresponds to the zonal moist static energy transport induced by the zonal anomalies of the turbulent fluxes and radiative cooling.

These experiments provide some hints to understand a few robust changes of the atmospheric circulation simulated by ocean-atmosphere coupled models for future and past climates.

1. Introduction

The tropical atmospheric circulation is characterized by mean ascending and subsiding motions in the troposphere. The mean ascents are located over areas of convective instability, in the Inter-Tropical Convergence Zone (ITCZ). Mean subsiding motion occurs over the subtropics, with strato-cumulus decks over oceans and deserts on land. The subsiding motions are partly governed by the emission of longwave radiations, evacuating partly the excess of Moist Static Energy (MSE) coming from the ascending regions (Pierrehumbert 1995). The subsidence in the subtropics is also governed by transient and stationary eddies (Trenberth and Stepaniak 2003). In the low troposphere, surface winds transport moisture from the subtropics, where oceanic evaporation is strong, to the ITCZ. Water vapor then condensates in convective clouds and the associated latent heat release provides the energy for the ascent and acts to maintain the dry static stability of the tropical free troposphere (Emanuel et al. 1994).

The tropical large scale circulation is commonly decomposed into zonal-mean and meridional-mean components, i.e. the Hadley and Walker circulations, both governed by different dynamics.

The Hadley cells act to transport angular momentum poleward, as shown in nearly inviscid axisymmetric models (Held and Hou 1980; Lindzen and Hou 1988). The presence of zonal asymmetries in the atmosphere creates eddies of different scales, especially in the midlatitudes. A large part of the Hadley circulation is also forced by these eddies (Schneider 2006). In the absence of eddies, idealized axisymmetric model simulations revealed that the Hadley cells are 75% weaker (Kim and Lee 2001). In fact, the eddies strengthen the Hadley

cells through the explicit eddy fluxes and also through their interaction with other processes such as the diabatic heating or surface friction. The Hadley circulation is fundamental for the atmospheric general circulation, as it transports MSE polewards, in addition to the transport realized by the transient and stationary eddies (Frierson et al. 2007; Frierson 2008). In the tropics, the MSE flux results from the compensation between the latent heat and Dry Static Energy (DSE) fluxes (Manabe et al. 1975). The atmospheric circulation, together with the radiation and surface turbulent fluxes, adjust so that the poleward MSE flux is in equilibrium with the incoming and outgoing energy into the atmosphere (Stone 1978).

The Walker circulation is mostly governed by the zonal SST-gradient across the equatorial Pacific Ocean (Yano et al. 2002). The zonal SST-gradient is the result of complex ocean-atmosphere interactions and of the tropical ocean dynamics controlling upwellings in the eastern sides of the oceanic basins. The Walker circulation is involved in the Bjerknes feedback that determines the characteristics of the El Niño Southern Oscillation (ENSO). Note also that both the Hadley and Walker circulations are strongly modulated by monsoon dynamics (Tanaka et al. 2004).

It has been demonstrated in a number of studies that the Hadley circulation was amplified in model simulations of the last glacial maximum (Broccoli et al. 2006), due to an amplified meridional SST gradient. On the other hand, paleo-proxies also revealed periods when the meridional SST gradients were extremely low, such as early Paleogene or Cretaceous. Modeling studies suggested furthermore that there was an atmospheric circulation very different from that of present-day climate (Huber 2009; Kump and Pollard 2008).

In most of the state-of-the-art ocean-atmosphere coupled models, the atmospheric large-scale tropical circulation weakens in response to increasing greenhouse gases concentration

in the atmosphere (Vecchi and Soden 2007). Within the free troposphere, the dry static stability increases more than the radiative cooling does, which causes a weakening of the subsidence in a warmer climate (Knutson and Manabe 1995). Over the ascending regions, Held and Soden (2006) showed that the large scale circulation weakens as a result of the changes in precipitation and water vapor in the atmosphere. The increase in precipitation is the result of relatively small changes in the radiation and surface energy budgets, while the atmospheric humidity increases at a larger rate following the Clausius-Clapeyron equation. The large scale circulation weakens so that the precipitation and moisture convergence within the boundary layer increase at a smaller pace than the water vapor increase.

The atmospheric circulation changes are not uniform, and the Hadley and Walker circulations experience different changes under global warming conditions. The Walker circulation weakens strongly in climate change projections (Vecchi and Soden 2007). Ocean-atmosphere coupled models also reveal a gentle decrease of the Hadley circulation strength (Gastineau et al. 2008), but the Hadley circulation weakening is found to be smaller than the associated weakening of the Walker circulation (Held and Soden 2006; Vecchi and Soden 2007). Previous studies, using Sea-Level-Pressure (SLP) observations, also suggest that the Walker circulation experienced a strong weakening in the recent period (Zhang and Song 2006; Vecchi et al. 2006), while reanalysis data show a strengthening of the boreal winter Hadley cell (Mitas and Clement 2005). Obviously, the Hadley and Walker circulations are driven by different mechanisms.

This paper studies the mechanisms governing the Hadley and Walker circulations and investigates the behaviors expected from different idealized changes in SST. The atmospheric circulation is studied in aqua-planet simulations using a full-physics GCM. The aqua-planet

configuration leads to simplified circulations. For instance, the absence of continents or mountains suppresses the monsoons. Also, the role of the sea-ice and ice caps is not taken into account. In the present study, aqua-planet simulations are set to reproduce both the Hadley and Walker circulations characteristics of present, past and future climates. Section 2 presents the methodology and the experimental design. Section 3 shows the main results concerning the large-scale circulation in the aqua-planet simulations. Section 4 is dedicated to a study of the zonal momentum. Section 5 focuses on the MSE budget. Section 6 provides a discussion and draws conclusions.

2. Model and simulations

The atmospheric GCM LMDZ4 is run without land and sea-ice. The GCM uses all its physical parametrizations, except for the parametrization of subgrid orography that was deactivated. LMDZ4 uses the convection scheme of Emanuel (1993), with a closure based on the convective available potential energy. The boundary layer is parametrized using K fluxes. LMDZ4 uses a finite-difference dynamical core, with an Arakawa C-grid and a rather low resolution of about $3.75^\circ \times 2.5^\circ$, with 19 levels in the vertical. The reader is referred to Hourdin et al. (2006) for an extensive presentation of the physical parameterizations of LMDZ4. The insolation conditions are set to a perpetual spring equinox, with the diurnal cycle being activated.

The initial conditions are obtained from a real state of the GCM. The removed orography is replaced by air masses having the same temperature as the surface. We perform a stabilized 60-month integration using the aqua-planet setting to deduce a stable initial state for all the

aqua-planet simulations. The duration of each simulation is 72 months, except for three simulations, that we extend up to 168 months. Note that we did not see any significant changes in the results by increasing the simulation length of these three simulations. The first 12 months of the simulations are discarded for the analysis.

The prescribed SSTs are partly derived from the *APE* protocol described in Neale and Hoskins (2001a,b). Table 1 presents the analytic functions used to express the prescribed SST, and Fig. 1 gives the zonal-mean SST profiles. The REF (reference) experiment uses an axisymmetric SST that is a mean between a $\sin^2$ and $\sin^4$ meridional profile: this simulation approximates the conditions observed on earth in present-day climate. A first set of experiments is built with the same SST equatorial maximum, and polar minimum, but with different meridional SST gradients. The simulations use a weaker (stronger) SST gradient in the tropical latitudes, a stronger (weaker) SST gradient in the midlatitudes, and are referred to as GRAD-2 and GRAD-1 (GRAD+1 and GRAD+2) as the tropical SST gradients are strongly and moderately weakened (strengthened). These SST patterns are irrelevant for present-day or near-future climate evolutions. However, in past climate conditions, the meridional SST gradient between tropics and extra-tropics decreased during warm episodes such as early Paleogene or the Cretaceous (Kump and Pollard 2008) and increased during the last glaciations.

In order to get a more realistic Walker circulation in the aqua-planet simulations, some zonal asymmetries of the SST are introduced in a second set of simulations. A wave-shaped SST anomaly, centered above the equator, is added to the reference axisymmetric SST. The SST anomaly is expressed as :

$$T_a sin(n\lambda) cos\left(\frac{\pi}{2}\frac{\phi}{\phi_c}\right),$$

where λ and ϕ are the longitude and latitude, n is the zonal wavenumber, ϕ_c is the meridional extent of the SST anomaly and T_a is the amplitude of the SST anomaly (see Fig. 1). The SST anomalies are shaped as stationary equatorial Kelvin waves, with 1, 2 and 3 as zonal wavenumbers. These experiments are referred to as WAVE1, WAVE2 and WAVE3. An amplitude of $T_a = 3K$ and a 20° extent in latitude are chosen. As an illustration, the structure of the SST anomaly is given for WAVE3 in Fig. 1.

In future scenario simulations, most model projections show a reduction of the zonal SST gradient in the Pacific Ocean (Di Nezio et al. 2009). So an experiment with the amplitude of SST anomalies reduced by 50% is added, using 3 as a zonal wavenumber and an amplitude T_a of 1.5K. This simulation is referred to as 0.5WAVE3.

Lastly, in order to assess the consequences of the anthropogenic greenhouse gases increase, a third set of experiments is performed with a uniform +2K SST increase from the experiments REF, WAVE1, WAVE2 and WAVE3. These uniform warming simulations can be described as reasonable analogs of future climate changes, and are able to reproduce some of the robust effects of climate change, such as the water vapor increase (Cess and Potter 1988), or the weakening of the large-scale tropical circulation (Gastineau et al. 2009). These simulations are referred to as REF+2K, WAVE1+2K, WAVE2+2K and WAVE3+2K.

3. Description of main results

a. Effect of the meridional SST gradients

The zonal-mean precipitation rates in the aqua-planet simulations are shown in Fig. 1. In Fig. 1, as in the following figures, an average of the results corresponding to the Northern and Southern Hemispheres is displayed, as there are only few differences between the two hemispheres.

The reference simulation, REF, shows rather realistic precipitation values over the ITCZ, with an equatorial value of about 8 mm d^{-1}. The equatorial precipitation maximum is followed, poleward, by a dry region between 10° and 25° of latitudes, which covers the subtropical subsiding zones.

For the reference simulation REF, a weak double ITCZ structure is simulated as the precipitation maximum is located around 4°. This feature is common in most aqua-planet models for the same prescribed SST (Williamson and Olson 2003; Brayshaw et al. 2008). The surface moisture flux cannot provide enough moisture to sustain a wide equatorial ITCZ, and a precipitation minimum is simulated over the equator.

In the simulations with amplified tropical SST gradients (GRAD+1 and GRAD+2), the ITCZ structure presents a single maximum, with heavy precipitations (14 and 20 mm d^{-1}). Conversely, the simulations with weakened tropical SST gradients (GRAD-1 and GRAD-2) show an over-amplified double ITCZ, with low precipitation rates over the equator.

Figure 2 illustrates the mean meridional streamfunction and the zonal-mean zonal wind. The simulation REF shows a rather strong Hadley circulation, with a maximum value of 17×10^{10} kg s^{-1}. The jet stream associated with the Hadley cell is also quite intense in REF,

with a jet core of about 60 m s^{-1}.

The simulations with strong meridional SST gradients (GRAD+1 and GRAD+2) all show a stronger Hadley circulation, with an intense jet stream. On the other hand, the simulations with weak meridional SST gradients (GRAD-1 and GRAD-2) have a weaker meridional streamfunction, whose maximum is far from the equator, at 25° for GRAD-2. In GRAD-2, the jet stream is located at 50°, far away from the Hadley cell. Furthermore, a zone without any significant zonal-mean circulation is observed at the center of the double ITCZ. In the following sections, we demonstrate that in the center of the double ITCZ, the radiative-convective equilibrium prevails, and no large-scale organization of the flow occurs.

The Hadley cell and jet stream are characterized by their strength and their latitudinal extent. The latitudinal extent of the Hadley cell is calculated as the latitude of the zero-value streamfunction, linearly interpolated, and averaged between 700-hPa and 300-hPa. The position of the jets is calculated as the latitude of the maximum zonal-mean zonal wind. The Hadley cell strength is given by the maximum absolute value of the streamfunction, averaged between the 700-hPa and 300-hPa heights, while the jet stream intensity is given by the maximum zonal-mean zonal wind. The results are illustrated in Fig. 3.

The Hadley cell is clearly stronger when the tropical SST gradient is increased, although the intensification with increased tropical gradient is much smaller than the weakening with decreased tropical gradient. The expansion of the Hadley cell is closely correlated to its strength. Indeed, the stronger the cell is, the narrower it is. A similar relation between strength and extent of the Hadley cell was observed in ocean-atmosphere coupled models by Lu et al. (2008). The jet stream intensity and position roughly correspond to those of the Hadley cell. Nevertheless, we illustrate in the next section that the strong SST gradients

over midlatitudes in GRAD-2 and GRAD-1 create a strong surface baroclinicity responsible for a reinforcement of the eddy-driven jet, which strengthens the jet and displaces it further poleward.

b. Effect of zonal SST anomalies

The simulations with zonal SST anomalies over the equatorial region (WAVE1,WAVE2 and WAVE3) have a single ITCZ with lower equatorial rainfalls (see Fig. 1). The subtropical rainfalls are enhanced compared to REF. In these simulations, the Hadley cell is weaker and wider compared to REF (see Figs. 2 and 3). The mean meridional streamfunction displays two distinct maxima located at 800-hPa and 350-hPa. The differences with REF increase in the low zonal wavenumber experiments.

In WAVE1, WAVE2 and to a lesser extent WAVE3, strong westerlies are simulated in the upper atmosphere above the equator. These strong westerlies show that the upper troposphere is in a state of superrotation. The superrotation is common in aqua-planet simulations (Suarez and Duffy 1992; Saravanan 1993; Battisti and Ovens 1995).

This superrotation is associated with the steady wave response to convection that settles over the warm SSTs. It is outside the scope of this paper to study the superrotation, but as the superrotation impacts the large scale tropical circulation, the three dimensional structure related to the steady wave structure is briefly illustrated in Fig. 4, for the WAVE2 simulation. The geopotential height and wind anomalies in the upper troposphere show anticyclonic (cyclonic) flows at low latitude over both hemispheres over the warm (cold) SSTs. The steady response is shaped like an equatorial Rossby wave with a weak Kelvin

wave component. The momentum flux by stationary eddies is oriented equatorward, thus transporting momentum from the midlatitudes to the equator, which contributes to the superrotation. The Hadley cell intensifies in the upper levels to compensate for the strong momentum flux by stationary eddies, which causes the upper-level maximum of the mean meridional streamfunction, between 400-hPa and 300-hPa, in Fig. 2.

The upper-tropospheric flow associated to the WAVE1 and WAVE3 simulations is shown in Fig. 5. The stationary wave pattern is amplified in WAVE1 compared to WAVE3, especially the Kelvin wave component. The superrotation is amplified for smaller zonal wavenumber, and the amplitude of the stationary wave pattern is substantially stronger when the zonal wavenumber decreases. It has been recognized in other studies that the Madden Julian Oscillation exhibits a preferential zonal scale of wavenumber one or two (Wang and Chen 1989), because of interactions between boundary-layer moisture convergence and latent heat release in the mid-troposphere.

The Walker circulation is first quantified by the velocity potential at the 200-hPa level, χ_{200}. The velocity potential reflects the large scale features of the tropical circulation, and is calculated using the horizontal wind at the 200-hPa level, following the definition:

$$\nabla.\mathbf{v}_{200} = -\nabla^2\chi_{200} \tag{1}$$

where $\mathbf{v}_{200}$ is the velocity vector at the 200-hPa height. A positive (negative) velocity potential at 200-hPa corresponds to regions of upper-tropospheric convergence (divergence).

The velocity potential of the simulations with zonal SST anomalies is shown in Fig. 6. The velocity potential anomalies reach 80×10^5 to 120×10^5 m^2 s^{-1}, which corresponds well

to the values found in reanalysis (Tanaka et al. 2004). In the WAVE simulations, the regions of upper-tropospheric divergence are located in the deep tropics, between 15°N and 15°S, over the warm SST regions. Regions of convergence develop in both hemispheres, between 20° and 40°, to the west of the main equatorial updrafts, as expected from the Gill model response to a prescribed heating (Gill 1980). The upper-tropospheric circulation above the equator, between 25°N and 25°S, is stronger when the zonal wavenumber increases.

The Walker circulation mass-flux is also calculated, to allow comparison with the meridional streamfunction that conventionally measures the Hadley cell strength. A mass-flux can be calculated within the domain of the Hadley circulation, since the zonal-mean mass flux is zero at the meridional boundaries of the Hadley cell. In this paper, the extent of the Hadley cells is computed on a monthly basis, in both the Northern and Southern Hemispheres, as the latitude of the zero-value mean meridional streamfunction, averaged between 700-hPa and 300-hPa. Then, a monthly zonal streamfunction is retrieved. The zonal streamfunction is strongly sensitive to the vertical shear of the mean zonal wind, characterized by easterlies at lower levels and westerlies at upper levels in the tropics. The zonal streamfunction circulation is also sensitive to the superrotation. Instead, we use the zonal anomalies of the zonal mean streamfunction, ψ_x^*, which provide a better diagnostic of the Walker circulation (see Appendix A).

Figure 7 shows the zonal streamfunction anomalies, ψ_x^*, in the domain of the Hadley cells. The Walker circulation is the strongest for WAVE1, where the maximum streamfunction, averaged between the 700-hPa and 300-hPa heights, is 9.8×10^{10} kg s^{-1}. If the zonal wavenumber increases, the Walker circulation intensity decreases, while the Hadley circulation intensity increases (see Fig. 3). The situation on Earth is similar to WAVE1, as only

two main cells are observed, even if the intensity is more similar to that of WAVE2 (see Appendix A).

c. Effect of uniform SST warming

The changes in the meridional streamfunction, between the +2K and control experiments, are represented in Fig. 8. All uniform warming simulations show a poleward expansion of the Hadley cell. This is illustrated by a positive streamfunction anomaly around 25° at the extra-tropical edge of the Hadley cell, followed by a negative anomaly around 40°. The tropopause pressure level is shifted upward by about 8 Pa in all +2K simulations. It explains the positive streamfunction anomaly above 200 hPa, seen in the tropics. However, the changes of meridional circulation between 0° and 15° are less systematic: the Hadley cell weakens in REF+2K, while it strengthens in the WAVE simulations. We also notice that in the WAVE simulations, the upper-level maximum of the meridional streamfunction weakens, between 400-hPa and 300-hPa.

The changes in the streamfunction maximum, averaged between 700-hPa and 300-hPa, are illustrated in Table 2. The simulation REF shows a gentle weakening of the Hadley circulation of -4.0%, while the Hadley cell strengthens by about 3% for the WAVE simulations. We compute the significance of the changes with a student t-test, where the degree of freedom was calculated using the total number of monthly outputs, to give a first order approximation of the significance. The Hadley cell changes in the +2K simulations are mostly significant, with p-values lower than 0.05, except for WAVE3 where the changes are smaller and insignificant.

The Walker circulation changes are illustrated with the changes of the velocity potential at 200-hPa (Fig. 6) and zonal streamfunction (Fig. 7). If we focus on the maximum value of the zonal streamfunction, the zonal streamfunction clearly strengthens in WAVE1 and to a lesser extent in WAVE2, while the changes are less obvious for WAVE3. On the other hand, the velocity potential changes depend on the region considered. The ascending branches are displaced westwards from the SST maximum for WAVE2 and WAVE3 in Fig. 7. Large differences are simulated in each wavelength, for instance in WAVE3 the changes at 60°E-180°E are small compared to those at 180°W-60°W. Those differences are due to the important internal variability in the simulations. Note that the increase of the duration of WAVE1, WAVE3 and WAVE3+2K, up to 168 months, does not improve the significance of these changes.

An analysis of the Walker circulation is presented in Table 2. The Walker circulation strength is first computed using the maximum absolute value of the zonal streamfunction, averaged between 700-hPa and 300-hPa, and over all extreme values. For instance, WAVE2 displays two maxima and two minima, and the Walker circulation strength is calculated as the average of the absolute values of these four extrema. Since previous studies of the Walker circulation under global warming conditions mainly use the velocity potential (Tanaka et al. 2004) or SLP (Vecchi et al. 2006; Vecchi and Soden 2007), we also measure the Walker circulation strength by the 200-hPa velocity potential and SLP gradients, within the deep tropics. We compute the mean difference of the velocity potential and SLP, between ascending and subsiding regions, averaged between 5°N and 5°S. An average over all wavelengths is shown for WAVE2 and WAVE3.

In Table 2, the response of the Walker circulation to a uniform warming is often small and

weakly significant. The zonal streamfunction increases in WAVE1, without any significant changes of velocity potentials or SLP gradients. WAVE2+2K shows a weakly significant intensification of the zonal streamfunction and a decrease in the equatorial velocity potentials, while in WAVE3+2K only the equatorial SLP gradient decreases. The zonal streamfunction represents the zonal circulation over the whole tropics, while the velocity potential and the SLP gradients, averaged between 5°N and 5°S, represent the circulation in the deep tropics. As the circulation changes in response to a uniform SST warming depend on the region considered, these diagnostics give different results. The response also varies depending on the zonal-wavenumber. For example, the Walker cells strengthen in WAVE1, while WAVE3 shows a weakening. In our simulations, the Walker circulation changes induced by a uniform SST warming are clearly small compared to the important weakening seen in models or observations, where both the velocity potential and SLP gradient decrease (Tanaka et al. 2004; Vecchi et al. 2006; Vecchi and Soden 2007).

d. Effects of the zonal SST gradients

The consequences of decreasing zonal SST gradients are investigated with a comparison of WAVE3 and 0.5WAVE3, as the zonal SST gradients are 50% weaker in 0.5WAVE3. The superrotation is weaker in 0.5WAVE3 than in WAVE3, and the stationary wave response is smaller (not shown). The 0.5WAVE3 experiment simulates an intensified Hadley circulation of +8.2% compared to WAVE3 (see Fig. 8). The Hadley cell is narrower, with a lower tropopause. The Walker cells weaken over the deep tropics, between 10°N and 10°S, where the ascending branches widen (see Figs. 6 and 7). All diagnostics in Table 2 show that

the Walker cells weaken compared to WAVE3, the zonal streamfunction decreases by -8.8%, and the velocity potential gradient decreases by -15.0%. The zonal SLP gradients are 50% smaller, as expected from the 50% reduction of the SST anomalies (Lindzen and Nigam 1987).

These changes correspond well to the changes of the Hadley and Walker circulation induced by ENSO. During El Niño (La Niña) events, warm (cold) SST anomalies in the Central and Eastern Pacific Ocean decrease (increase) the zonal SST gradients, which results in a weakening (strengthening) of the Walker cells and a strengthening (weakening) of the Hadley cell (Oort and Yienger 1996). Surprisingly, the changes induced by a modification of the zonal SST gradient are stronger and more significant than those simulated by a uniform SST warming (see Table 2). Therefore, the modifications of the zonal SST gradient in simulations with complete ocean-atmosphere coupled models could play a major role in explaining the changes of the Hadley and Walker cells.

e. Thermodynamical state of the tropical atmosphere

Our simulations give a large variety of dynamic and thermodynamic states in the tropical troposphere. Figure 9 depicts the mean tropical thermodynamic state of the tropical troposphere in our experiments, with the dry static stability at 500-hPa, Sp_{500}, the precipitation, P, the column integrated water vapor, W, and the 500-hPa mean ascending velocities, M^{+}_{500}. The dry static stability Sp_{500} is equivalent to the Brunt Väisälä frequency, and is defined as:

$$Sp = -\frac{T}{\theta}\frac{\partial \theta}{\partial p}$$

The ascending mid-tropospheric vertical velocity at the 500-hPa height, M_{500}^{+}, measures the large scale circulation intensity, computed using the ascending grid points only. This quantity is proportional to the mean convective updraft velocity (Vecchi and Soden 2007). Note that all quantities in Fig. 9 are averaged over the domain of the Hadley cells, as defined in Section 3.b.

All simulations are consistent with the robust changes of the models in global warming conditions, reviewed by Held and Soden (2006). Throughout the simulations, the lower-tropospheric relative humidity is relatively constant (not shown). Thus, the water vapor content in the atmosphere follows the Clausius-Clapeyron equation. For instance, the SSTs in GRAD-2 are larger than in GRAD+2 when averaged over the tropical region, thus the column integrated water vapor in GRAD-2 is also larger than in GRAD+2. The water vapor increase leads to an increase in the moisture flux convergence within the boundary layer in moist regions. However, the precipitation changes in most simulations are smaller than the water vapor changes, as the precipitation is more constrained by the radiative fluxes. Therefore, the mean ascending mass flux decreases with larger SSTs, in order to diminish the convergence of the moisture flux.

The dry static stability changes also agree with the robust changes of ocean-atmosphere coupled models, studied by Knutson and Manabe (1995) or Held and Soden (2006). The SST determines the moist lapse rate and dry static stability over the convective regions. The tropical regions have a uniform lapse rate, especially in the deep tropics, as a consequence of the small Coriolis parameter near the equator (Sobel et al. 2001). For warm SST over the convective regions, the water vapor and latent heating increase, which causes an increase in the tropical dry static stability. Over the subsiding regions, the subsidence, at the zeroth

order, is given by the ratio between the atmospheric radiative cooling and the dry static stability. The increase in dry static stability is accompanied by a smaller increase in radiative cooling (not shown), which leads to a weakening the tropical circulation.

However, these mechanisms do not apply for all simulations. For instance, WAVE3 shows a stronger dry static stability compared to REF, but the mean ascending velocities are stronger than REF. The changes of the mean ascending velocity are unable to quantify the large scale organization of the flow. It has been recognized that a widening of the area covered by ascending motions could induce a stronger circulation without modifications of the mean ascending velocity (Pierrehumbert 1995). Furthermore, the Hadley cells are expected to be governed by the SST meridional gradients (Held and Hou 1980; Gastineau et al. 2009). To further understand the changes of the large scale circulation, one needs to analyze the momentum and MSE budgets.

4. Mean zonal wind balance

The zonal-mean zonal wind shows a large variety of behaviors in our experiments. For instance, the simulations using a zonal SST anomaly present a superrotation in the upper tropical atmosphere. Another interesting phenomenon is observed in the simulations with a weak tropical meridional SST gradient, where the maximum zonal wind is shifted poleward with respect to the position of the Hadley cells. These singular behaviors can be explained by the zonal momentum balance.

The terms of the zonal-mean zonal momentum equation are calculated following the methodology used in Seager et al. (2003):

$$\frac{\partial \left[\overline{u}\right]}{\partial t} = -\left(\frac{\left[\overline{v}\right]}{a}\frac{\partial \left[\overline{u}\right]}{\partial \phi} + \left[\overline{\omega}\right]\frac{\partial \overline{u}}{\partial p}\right) + \left(f + \frac{\left[\overline{u}\right]\sin\phi}{a\cos\phi}\right)\left[\overline{v}\right]$$

$$-\frac{1}{a\cos^2\phi}\frac{\partial}{\partial\phi}\left(\left[\overline{u}^*\overline{v}^*\right]\cos^2\phi\right) - \frac{\partial}{\partial p}\left[\overline{u}^*\overline{\omega}^*\right] - \frac{1}{a\cos^2\phi}\frac{\partial}{\partial\phi}\left(\left[\overline{u'v'}\right]\cos^2\phi\right) - \frac{\partial}{\partial p}\left[\overline{u'\omega'}\right] - \overline{D\left[u\right]} \quad (2)$$

Here, square brackets indicate a zonal mean, asterisks indicate departure from the zonal mean, overbars indicate a monthly mean, and primes indicate departure from the monthly means. The variable u is the zonal wind, v, the meridional wind, ω, the vertical pressure velocity, a, the radius of the earth, p, the pressure, f, the Coriolis parameter, and $\overline{D\left[u\right]}$ is a damping. The first term on the right-hand side of Eq. (2) is the advection of the zonal-mean wind by the mean meridional circulation. The second term is the Coriolis torque. The third and fourth (respectively fifth and sixth) terms are the stationary (respectively transient) eddy flux convergence of zonal momentum.

The simulations are in a stationary state, therefore the time derivative is neglected. The damping term, calculated as a residual, is found to be very small in the upper troposphere, and is also neglected. The various terms of Eq. (2) are shown at the 200-hPa height in Fig. 10.

In the REF simulation, between 0° and 25° in latitudes, the Coriolis torque is mainly responsible for the acceleration of the zonal wind, as the zonal momentum is transported poleward by the Hadley cell. The mean advection acts to diminish the zonal wind in the tropics. The transient eddies also decelerate the wind in the subsiding branch of the Hadley cell, i.e. between 10° and 25°. Then, between 25° and 45°, in the Ferrel cell, the mean zonal wind is accelerated by transient eddies, while the Coriolis torque tends to slow it down.

In the simulation GRAD-2, all terms are small between 0° and 15°, and thus the zonal

wind is weak in the equatorial region. Between 15° and 30°, the Coriolis and mean advection terms are smaller compared to REF as the mean meridional circulation is weaker. The transient eddy momentum divergence is of a similar magnitude, but shifted polewards, between 10° and 30°. This term becomes much stronger in the midlatitudes, between 30° and 70°. This is related to the very strong midlatitude SST gradients, which increases the baroclinicity and the transport of momentum by transient eddies. These transient eddies give momentum to the zonal-mean zonal wind, which enhances the eddy-driven jet. A similar effect was obtained by Brayshaw et al. (2008) when the midlatitude SST gradients were specifically modified. The subtropical jet, that is more dependent on the momentum divergence by the mean meridional circulation, is decreased, as the Hadley cell is weak.

In WAVE3, the stationary wave pattern is clearly responsible for a convergence of momentum in the equatorial region, between 0° and 5°, where it causes the superrotation, as shown in Section 3.b. Elsewhere, the stationary eddy momentum flux is smaller than the other terms. The Coriolis and mean advection terms are smaller in WAVE3, as the Hadley cell is weaker. An analysis of WAVE1 or WAVE2 gives qualitatively similar results. The modifications of the zonal wind in WAVE3 are small beyond 30°, and the maximum zonal-mean zonal-wind is almost unchanged despite a large weakening of the Hadley cell.

The changes affecting the zonal-mean wind in our simulations correspond well to those of the transient and stationary eddies that displace and amplify the eddy-driven jets. The intensity of the Hadley cell is associated to the Coriolis torque and mean momentum advection terms. The locations of the maximum momentum flux convergence by the zonal-mean circulation and eddies are computed to illustrate the positions of the subtropical, ϕ_{STJ} ,and eddy-driven, ϕ_{EDD}, jets.

$$\phi_{STJ} \quad \text{where} \quad \frac{1}{a\cos\phi}\frac{\partial[\overline{u}][\overline{v}]\cos\phi}{\partial\phi} \quad \text{is maximum} \tag{3}$$

$$\phi_{EDD} \quad \text{where} \quad \frac{1}{a\cos\phi}\frac{\partial([\overline{u'v'}]+[\overline{u}^*\overline{v}^*])\cos\phi}{\partial\phi} \quad \text{is maximum} \tag{4}$$

These positions are added in Fig. 3. The eddy-driven jet is clearly responsible for the poleward displacement of the maximum zonal wind in GRAD-1 and GRAD-2, but also in the +2K simulations. In the +2K simulations, the Hadley cell expansion is analogous to that of ocean-atmosphere coupled models in global warming conditions (Lu et al. 2007). This extension is governed in these models by the increase of the dry static stability which prevents the penetration of midlatitude eddies into the tropics (Lu et al. 2008).

5. Budgets of moist static energy

In this section, the large-scale tropical circulation is analyzed through the moist static energy (MSE) variable. The MSE quantifies the energy transported by air parcels and is defined as $m = s + L_v q$, where $s = C_p T + gz$ is the DSE (Dry Static Energy) and $L_v q$ is the latent heat.

The column-average MSE budget is :

$$\nabla.(\overline{\mathbf{v}m}) = \overline{Q_R} + \overline{H} + \overline{L_v E}, \tag{5}$$

where $\mathbf{v}$ is the wind vector. The overbars designate monthly and vertical averaging. H the turbulent sensible heat flux, E the turbulent evaporation flux. Q_R is the net atmospheric radiative heating rate, diagnosed from the budget of the radiative flux at the surface and

top of the atmosphere.

a. Meridional transports of moist static energy

The zonal-mean budget of MSE is :

$$\frac{1}{a}\frac{\partial}{\partial\phi}[\overline{v}]\,[\overline{m}] + \frac{1}{a}\frac{\partial}{\partial\phi}\left[\overline{v'm'}\right] + \frac{1}{a}\frac{\partial}{\partial\phi}[\overline{v}^*\overline{m}^*] = \left[\overline{Q_R}\right] + \left[H\right] + \left[\overline{L_v E}\right]. \tag{6}$$

Here, the first term of the left-hand side of Eq. (6) is the MSE divergence by the zonal-mean circulation. The second and third terms are the MSE divergence by transient and stationary eddies.

The transport of MSE, and its division into zonal-mean and eddy components, were carefully diagnosed in the simulations, with an on-line diagnostic using the fields of wind, moisture and DSE at each physical time step of the GCM. We check that the MSE divergence of the total transport diagnosed (left-hand side of Eq. (6)) corresponds to the sum of the energy provided at the surface and top of the atmosphere (right-hand side of Eq. (6)), so that MSE is conserved in the model with our diagnostics.

As the DSE increases with height, the direction of its transport by the zonal-mean circulation depends on the upper level flow. In the tropics, the DSE is therefore transported poleward by the Hadley circulation, as illustrated in Fig 11. Conversely, the zonal-mean latent heat transport is mostly due to the lower troposphere, and is therefore directed equatorward. In the midlatitudes, the eddies transport both latent heat and DSE polewards, as shown in Fig. 11. Over the domain of the Hadley cells, the DSE and latent heat transports compensate giving a relatively small poleward MSE flux.

The MSE fluxes, and their decomposition into mean, stationary and transient components are given in Fig. 12. All simulations have a maximum energy flux located between 35° and 40°, with a similar intensity. GRAD+2 (GRAD-2) shows an amplified (reduced) poleward energy flux in the tropics. The differences among the total MSE flux of the simulations REF, REF+2 and WAVE are smaller.

The MSE budget is further illustrated in Fig. 13, by the different terms at the right-hand side of Eq. (6). In REF, between the equator and 35°, the evaporation and, to a lesser extent, sensible heating, provide MSE to the atmosphere, while the radiative cooling emits a smaller part of that energy towards space. The MSE fluxes are divergent. Beyond 35°, the loss of energy due to radiative cooling is the dominant term, and the MSE fluxes are convergent.

In GRAD+2, between 0° and 5°, the evaporation provides a large amount of energy at the surface while the radiative cooling is not strong enough to compensate. A vigorous Hadley circulation transports a large amount of MSE toward the poles. Conversely, between 5° and 40°, the latent heat flux is smaller than in REF and the exported MSE from this region decreases. In GRAD+2, this evaporation increase could be explained by the Wind-Induced Surface Heat Exchange (WISHE) that may act as a positive feedback and strengthen the large-scale circulation (Numaguti 1993, 1995; Boos and Emanuel 2008). However, another set of simulations with prescribed surface fluxes needs to be performed to properly document the role of WISHE.

In GRAD-2, between 0° and 10°, the MSE provided by the turbulent fluxes is nearly equal to the radiative cooling. Therefore, the Hadley circulation is negligible and the radiative-convective equilibrium prevails. However, between 15° and 30°, the evaporation is strong and

the MSE flux strengthens. The transient eddy MSE flux mainly accounts for this stronger MSE flux.

In the WAVE3 or REF+2K simulations, more energy is provided by the turbulent fluxes at the surface. For REF+2K the turbulent fluxes are stronger everywhere, while for WAVE3, the changes are confined to the equatorial region. In both simulations, a stronger radiative cooling occurs at the same latitudes, and the energy excess is radiated to space. Therefore, the MSE fluxes are only weakly modified in these simulations.

b. Zonal transport of Moist Static Energy

The MSE budget (Eq. (6)) is averaged over the domain of the Hadley cells :

$$\langle \nabla.(\overline{\mathbf{v}m}) \rangle = \langle \overline{Q_R} \rangle + \langle \overline{H} \rangle + \langle \overline{L_v E} \rangle \tag{7}$$

where angle brackets indicate the average over the domain of the Hadley cells (see Section 3.b). Here, the term on the left-hand side describes the total MSE divergence, due to the Walker and Hadley circulations (i.e. $\langle \nabla.(\overline{\mathbf{v}}\ \overline{m}) \rangle$) and transient eddies (i.e. $\langle \nabla.(\overline{\mathbf{v}'m'}) \rangle$). The right-hand side terms describe the energy provided in the Hadley cells domain by radiative cooling, sensible and latent heat fluxes.

The zonal anomalies of the terms on the right-hand side of Eq. (7) are shown in Fig. 14, for the simulations WAVE1, WAVE1+2K, WAVE3, WAVE3+2K and 0.5WAVE3. Over the cold (warm) SST anomalies, the radiative cooling and turbulent fluxes present large negative (positive) anomalies. As a consequence, the Walker circulation transports MSE directly from the warm SST regions to the cold ones. The zonal anomalies of the mean

meridional circulation and eddies also contribute to this MSE transport.

In WAVE1+2K, the zonal gradient of latent heat flux increases as a response to the SST warming. The increase of the latent heat flux is mainly due to the exponential dependence of the saturation water vapor pressure on temperature, following the Clausius-Clapeyron relationship. The increase of evaporation is stronger over the warm SST regions. The large-scale atmospheric circulation transports more MSE and the Walker circulation strengthens. On the other hand, in WAVE3+2K, the increase in turbulent flux anomalies is less systematic, and the turbulent heat fluxes decrease over the warm SSTs located at 50°E or 150°E. These changes are associated with a gentle weakening of the Walker cells (see Table 2). The evaporation anomalies also decrease (increase) over the eastern (western) edge of the warm SST anomalies, which contributes to a westward shift of the ascending zones in Fig. 6. It can be concluded that the Walker cells intensity corresponds to the zonal gradient of turbulent heat flux. For a uniform SST warming, the changes of the turbulent heat flux depends on the pattern of the control SST.

In 0.5WAVE3, the anomalies between warm and cold regions are strongly reduced when compared to WAVE3. As the amplitude of the SST anomalies are reduced, the turbulent fluxes and radiative cooling anomalies are also smaller. The large-scale circulation transports less MSE from the warm regions to the cold ones. Therefore, the Walker cells weaken when the zonal SST gradients are reduced.

c. Role of moist static stability

The links between the MSE flux and the Hadley cell are complex. The mean meridional circulation transports an important part of the total MSE flux in the tropics, while eddies dominate in higher latitudes (see Fig. 12). In the tropics, the MSE transport is determined by the compensation between the DSE and latent heat fluxes (see Fig. 11). The gross moist static stability is commonly used to measure the ratio between the DSE and latent heat fluxes, and quantifies the efficiency of the MSE transport by the mean meridional circulation (Neelin and Held 1987). The gross moist static stability is associated with the geographical distribution of convection. It is also linked to the convection scheme used (Frierson 2007).

The gross moist static stability, Δm, is defined as the ratio between the zonal-mean MSE flux and the intensity of the meridional circulation :

$$\Delta m = \frac{\int_{P_s}^{0} [\overline{v}][\overline{m}]dp}{\int_{P_s}^{P_m} [\overline{v}]dp} \tag{8}$$

where the overbars denote a time averaging. P_s is the surface pressure. P_m is a mid-tropospheric level where the vertical velocity is maximum, commonly found around 500-hPa. The unit of the gross moist static stability is kJ kg^{-1}. It is the amount of MSE transported per kg of mean meridional mass circulation. The denominator on the right-hand side of Eq. (8) is the intensity of the meridional circulation. This formulation of the gross moist static stability is similar to that of Neelin and Held (1987), but follows the definition of Frierson et al. (2007) by defining it as a ratio of flux rather than flux divergence.

We define C, the ratio of the total MSE flux transported by the mean meridional circulation.

$$C = \frac{\int_{P_s}^{0} [\overline{v}][\overline{m}]dp}{F} \tag{9}$$

where F is the total zonal-mean MSE flux, defined as $\int_{P_s}^{0} [\overline{vm}]dp$. The ratio C quantifies the contribution of zonal mean circulation in the total MSE flux. An increase of eddy MSE flux for the same total MSE flux leads to a reduced ratio C. We find a simple relation, analogous to Kang et al. (2009) to describe the intensity of the meridional circulation:

$$\int_{P_s}^{0} [\overline{v}]dp = \frac{CF}{\Delta m} \tag{10}$$

The gross moist static stability, Δm, of the simulations is shown in Fig. 15. Furthermore, the gross moist static stability, Δm, the ratio C, and the total MSE flux, F, are estimated between 2.5° and 15°, where the mean meridional streamfunction is the strongest. The results are shown in Fig.16.

In the REF simulation, the poleward MSE flux is 1.1 PW. The Hadley cell is responsible for 28% of the total MSE flux. The gross moist static stability is quite small, i.e. 3.0 kJ kg^{-1}. As the deep tropical SSTs are warm, atmospheric convection is frequent, which homogenizes the MSE profiles ($\Delta m \approx 0$).

In the amplified tropical SST gradient simulations (GRAD+1 and GRAD+2), the total MSE flux increases, as the evaporation provided in the deep tropics increases (see Fig. 13), which strengthens the Hadley cell. Nevertheless, the gross tropical moist static stability also increases, as most of the convection is located over the equator, while the region between 5° and 25° experiences less convection than REF (see precipitation in Fig. 1). Therefore, the Hadley cell intensity is only weakly enhanced.

In the reduced tropical gradient simulations (GRAD-2 and GRAD-1), the Hadley cells are displaced into the midlatitudes. The total MSE flux is much lower than REF in the deep tropics. The Hadley circulation is negligible in the deep tropics as the radiative-convective equilibrium prevails over such weak SST gradient conditions (Held and Hou 1980). Note that for the experiment GRAD-1, an inverse weak overturning cell appears in the deep tropics, causing negative values of the gross moist static stability in Figs. 15 and 16. In these simulations, the Hadley cells are located in the midlatitudes (around 25° for GRAD-2), where the moist static stability is larger than in the deep tropics, which further weakens the Hadley cells.

In the simulations with zonal SST anomalies (WAVE1, WAVE2, WAVE3 and 0.5WAVE3), some subsiding motions occurs in the deep tropics, as convection is inhibited over the cold SST regions (see Fig. 6). Therefore, the zonal-mean gross moist static stability increases over the deep tropics compared to REF (see lower panel of Fig. 15). The total MSE flux increases in these simulations (Fig. 16), but the increase in gross moist static stability is stronger, so that the mean meridional circulation weakens. In the high zonal wavenumber simulations, such as WAVE3, the zonal SST gradient is locally stronger than in the low wavenumber cases (i.e. WAVE1), and the turbulent fluxes are enhanced by strong low-level winds. The reinforcement of the total MSE flux may explain the strengthening of the Hadley cells when the zonal wavenumber increases.

In the +2K simulations, the total MSE transport is almost invariant (see Figs. 12 and 15). All simulations show a decrease of the deep tropical gross moist static stability. This decrease is associated with the moistening of the lower troposphere, which exceeds the increase of dry static stability in the upper troposphere. This effect is compensated by a decrease of C, the

fraction of the total MSE flux performed by the mean meridional circulation (see Fig. 16), which corresponds to a reinforcement of the eddy component of the MSE flux. In REF, the decrease of C prevails, while in the WAVE simulations, the changes of the gross moist static stability are larger. We conclude that the Hadley circulation changes induced by a uniform SST increase are highly dependent on the pattern of the control SST, as it determines the changes resulting from the eddy MSE flux and gross moist static stability.

6. Discussion and conclusion

The parameters that determine the strength of the Hadley and Walker circulation in a GCM are studied through various idealized aqua-planet simulations, using a GCM with a comprehensive physical package. Four types of simulations are studied : (1) simulations with axisymmetric SSTs where the meridional SST gradient is modified; (2) simulations with a longitudinal equatorial wave-shaped SST anomaly; (3) uniform warming simulations of 2K; (4) simulations where the equatorial zonal SST gradient is modified.

Drastic changes are seen when the meridional SST gradient is modified. A SST profile with a maximum peaked at the equator produces a strong Hadley circulation, with a small extent accompanied by a strong jet. For large tropical SST gradients, a vigorous Hadley circulation is expected from the classical angular momentum framework. As convection settles in the vicinity of the equator, the tropical gross moist static stability increases, which lessens the Hadley cells intensification. Nevertheless, as our simulations use fixed SST conditions, evaporation anomalies can increase without an accompanying SST decrease, and the Hadley cell intensity may have been overestimated. This case of strong and narrow Hadley cell

shares some characteristics with the climate of the last glacial maximum (Williams 2006; Broccoli et al. 2006).

In the case of a very flat SST distribution at the equator, a double ITCZ is simulated. The Hadley cells are very weak with a large spatial extent. As the radiative-convective equilibrium is possible, the classical angular momentum theory predicts that no large scale organization of the flow occurs in the tropics (Held and Hou 1980). In this case, the Hadley cells and MSE flux are governed by eddy dynamics. As very strong meridional SST gradients are located in the midlatitudes, the midlatitude baroclinicity increases and the eddy-driven jet is enhanced. It is likely that an analogous circulation existed during warm episodes of past climate, such as the Eocene or the late Cretaceous, even if it is still unclear how such SST gradients can be sustained by ocean-atmosphere coupling.

A significant weakening of the Hadley cell is induced by the introduction of the SST wave-shaped anomaly. Such a configuration induces a superrotation in the upper-troposphere and the formation of stationary eddies in the tropics. In addition, the gross moist static stability increases, as convection is inhibited over the tropical subsiding zones. The poleward MSE transport by the Hadley cells is more efficient, without any modifications of the total MSE fluxes, and therefore the Hadley cells slow down. The superrotation is a caveat in our simulations, as such a state is not observed in present-day climate. The presence of superrotation may be due to the absence of cross equatorial SST gradient in perpetual equinox conditions (Kraucunas and Hartmann 2005) and it would be interesting to repeat our experiments in the case of the solstices. However, the mechanisms that weaken the Hadley cells in the presence of longitudinal SST anomalies are still valid for present-day climate.

A uniform warming of +2K induces non-systematic modifications of the Hadley and Walker circulations, even if the mean updraft velocity diminishes in all simulations. A uniform warming of +2K leads to a weakening of the Hadley cells in the reference simulation, due to an enhancement of the MSE flux by transient eddies. With the introduction of a warm pool and a cold SST region, the Hadley circulation increases in the case of a warming, due to a decrease of moist static stability. Therefore, the Hadley circulation induced by a uniform SST warming depends on the control SST pattern, which determines characteristics of the transient and stationary eddy fluxes. On the other hand, the Walker circulation increases (decreases) in the simulation with a zonal wavenumber 1 (3) and the reasons for these different changes are still to be rigorously established. We suggest that the evaporation anomalies are enhanced in our uniform warming simulations, which enhances the Walker cells. In the case of a high zonal wavenumber, the Walker cells may also be affected by changes in the transient and stationary eddy flux divergence of MSE.

The weakening of the zonal equatorial SST anomalies causes a weakening of the Walker cells and a strengthening of the Hadley cells. The Hadley cells strengthen mainly because the zonal-mean gross moist static stability diminishes, as the ascending branches are wider and convection is more uniformly distributed over the tropics. The weakening of the Walker cells corresponds well to the decrease of MSE provided by the anomalous turbulent fluxes in the tropics.

Aqua-planet simulations represent simple intermediate-complexity tools suitable for studying the atmospheric dynamics. Such simulations show a lot of deficiencies such as the double ITCZ or superrotation. But the simplicity of these experiments also allows us to isolate a few mechanisms that may have modified the tropical large-scale circulation in past- or future-

climate SSTs. Such processes are more difficult to detect in realistic situations because of the complexity introduced by orography, land-ocean contrasts or non-linearities associated with the seasonal cycle (Lindzen and Hou 1988).

In a global warming scenario, ocean-atmosphere coupled models, or models coupled to an ocean mixed-layer, show a strong weakening of the Walker circulation (Vecchi and Soden 2007), while the Hadley cells only show a gentle decrease (Vecchi and Soden 2007; Gastineau et al. 2008). In our simulations, such changes are not obtained with uniform SST warming. How can we explain these differences? We suggest three explanations:

- Firstly, the fixed SST lower boundary conditions in our simulations could lead to unrealistic values of the evaporation and cloud changes, as the SST is not allowed to interact with the atmosphere. The surface turbulent flux and the clouds are expected to be different in coupled ocean-atmosphere models, which can affect the Hadley and Walker circulations.

- Secondly, the stationary and transient eddies are obviously unrealistic in our simulations, due to the absence of continents and mountains, and the eddies through their interactions with the diabatic and friction processes play a crucial role in driving the Hadley cells (Kim and Lee 2001).

- Lastly, we also argue that the weaker Pacific Ocean zonal SST gradient simulated by most ocean-atmosphere coupled models in global warming conditions may govern part of the Walker circulation weakening. It may also explain the different changes of the Hadley and Walker cells in ocean-atmosphere coupled models. When the zonal SST gradient decreases, we find a weakening of the Walker cells and a strengthening of the

Hadley cells. Such an effect is analogous to that observed during El Niño events in observations (Oort and Yienger 1996). However, the decrease of the SST gradient in the Equatorial Pacific Ocean obtained in ocean-atmosphere coupled models (≈ 0.5°K) is relatively low compared to the applied 3°K decrease of the SST gradient in our simulations.

The tropical large scale circulation response simulated by the ocean-atmosphere coupled models is not fully reproduced by our aqua-planet simulations, although they include the water vapor and dry static stability changes. This is a clear demonstration that our understanding of these circulations is not sufficient and requires more study.

Acknowledgments.

This work was supported by a PhD grant from the Université Pierre et Marie Curie, Paris, France. We thank Dargan M.W. Frierson, and two anonymous reviewers who contributed to improve this manuscript.

APPENDIX A

The zonal streamfunction anomalies as a diagnostic of the Walker cells

As we introduce a new diagnostic to study the Walker cells, this appendix provides some details on the calculation of this diagnostic.

Within the Hadley cells domain, the mass circulation is closed and the mean mass flux is zero at the Hadley cell boundaries. We calculate the extent of the Hadley cells on a monthly basis, given by the zero-value mean meridional streamfunction, averaged between 300-hPa and 700-hPa. The Hadley cell extents in the Northern Hemisphere, ϕ_N, and in the Southern Hemisphere, ϕ_S, are separately retrieved. The zonal wind is averaged between these two latitudes:

$$\langle u \rangle = \frac{1}{\phi_N - \phi_S} \int_{\phi_S}^{\phi_N} u d\phi, \tag{A1}$$

where angle brackets denote an averaging over the domain of the Hadley cells. The zonal streamfunction in the Hadley circulation region, ψ_x, is expressed as :

$$\psi_x = a \frac{(\phi_N - \phi_S)}{g} \int_{p_s}^{p} \langle u \rangle dp, \tag{A2}$$

where a is the earth radius, g, the gravity acceleration, p_s the surface pressure and p the pressure. From the zonal streamfunction, two components are retrieved :

$$\psi_x = [\psi_x] + \psi_x^* \tag{A3}$$

where square brackets indicate zonal averaging, and asterisks designate zonal anomalies. $[\psi_x]$ is proportional to the vertical shear of the zonal-mean zonal wind. The residual ψ_x^* represents the Walker circulation . Figure 17 shows the zonal-mean zonal streamfunction, $[\psi_x]$, and the zonal streamfunction anomalies, ψ_x^*, from the ERA40 reanalysis (Uppala et al. 2005), during the 1979-2001 period.

Strong ascending motions are located over the western Pacific Ocean. Weaker and narrower ascents are located over the eastern Pacific, Atlantic and Indian Ocean, therefore the anomalous zonal circulation shows some subsiding motions over these regions.

Note that the use of an average between 25°N and 25°S, instead of an average over the domain of the Hadley cells, provides similar results. So these results are not sensitive to the precise definition of the latitudes used to delimit the Walker circulation.

REFERENCES

Battisti, D. S. and D. D. Ovens, 1995: The dependence of the low-level equatorial easterly jet on Hadley and Walker circulations. *J. Atmos. Sci.*, **52**, 39113931.

Boos, W. R. and K. A. Emanuel, 2008: Wind-evaporation feedback and abrupt seasonal transition of axisymmetric Hadley circulation. *J. Atmos. Sci.*, **65**, 2194–2214.

Brayshaw, D., B. Hoskins, and M. Blackburn, 2008: The storm-track response to idealized SST perturbations in an aquaplanet GCM. *J. Atmos. Sci.*, **65 (9)**, 2842–2860.

Broccoli, A. J., K. A. Dahl, and R. J. Stouffer, 2006: Response of the ITCZ to Northern Hemisphere cooling. *Geophys. Res. Lett.*, **33**, L01 702, doi:10.1029/2005GL024 546.

Cess, R. D. and G. L. Potter, 1988: A methodology for understanding and intercomparing atmospheric climate feedback processes in general circulation models. *J. Geophys. Res.*, **93**, 8305–8314.

Di Nezio, P. N., A. Clement, G. Vecchi, B. Soden, B. Kirtman, and S.-K. Lee, 2009: Climate Response of the Equatorial Pacific to Global Warming. *J. Climate*, **22**, 4873–4892.

Emanuel, K. A., 1993: A cumulus representation based on the episodic mixing model: the importance of mixing and microphysics in predicting humidity. *AMS Meterol Monogr*, **24 (46)**, 185–192.

Emanuel, K. A., J. D. Neelin, and C. S. Bretherton, 1994: On large-scale circulations in convecting atmospheres. *Q. J. R. Meteorol. Soc.*, **120 (519)**, 1111–1143.

Frierson, D. M. W., 2007: The dynamics of idealized convection schemes and their effect on the zonally averaged tropical circulation. *J. Atmos. Sci.*, **64**, 1959–1976.

Frierson, D. M. W., 2008: Midlatitude static stability in simple and comprehensive general circulation models. *J. Atmos. Sci.*, **65**, 1049–1062.

Frierson, D. M. W., I. M. Held, and P. Zurita-Gotor, 2007: A gray-radiation aquaplanet moist GCM. Part II: energy transports in altered climates. *J. Atmos. Sci.*, **64**, 1680–1693.

Gastineau, G., H. L. Treut, and L. Li, 2008: Hadley circulation changes under global warming conditions indicated by coupled climate models. *Tellus A*, **60 (5)**, 863–884.

Gastineau, G., H. L. Treut, and L. Li, 2009: The Hadley and Walker circulations changes in global warming conditions described by idealized atmospheric simulations. *J. Climate*, **22**, 3993–4013.

Gill, A. E., 1980: Some simple solutions for heat induced tropical circulations. *Q. J. R. Meteorol. Soc.*, **106**, 447–462.

Held, I. M. and A. Y. Hou, 1980: Nonlinear axially symmetric circulations in a nearly inviscid atmosphere. *J. Atmos. Sci.*, **37**, 515–533.

Held, I. M. and B. J. Soden, 2006: Robust responses of the hydrological cycle to global warming. *J. Climate*, **19**, 5686–5699.

Hourdin, F., et al., 2006: The LMDZ4 general circulation model: climate performance and sensitivity to parametrized physics with emphasis on tropical convection. *Clim. Dyn.*, **27**, 787–813.

Huber, M., 2009: Climate change: Snakes tell a torrid tale. *Nature*, **457**, 669–671, doi:10.1038/457 669a.

Kang, S. M., D. M. W. Frierson, and I. M. Held, 2009: The tropical response to extratropical forcing in an idealized GCM: the importance of radiative feedbacks and convective parametrisation. *J. Atmos. Sci.*, **66**, 2812–2827.

Kim, H. K. and S. Y. Lee, 2001: Hadley cell dynamics in a primitive equation model. Part II: Nonaxisymmertic flow. *J. Atmos. Sci.*, **58**, 2859–2871.

Knutson, T. and S. Manabe, 1995: Time mean response over the tropical pacific to increased CO_2 in a coupled ocean-atmosphere model. *J. Climate*, **8**, 2181–2199.

Kraucunas, I. and D. Hartmann, 2005: Equatorial superrotation and the factors controlling the zonal-mean zonal winds in the tropical upper troposphere. *J. Atmos. Sci.*, **62**, 371–389.

Kump, L. R. and D. Pollard, 2008: Amplification of cretaceous warmth by biological cloud feedbacks. *Science*, **320 (5873)**, 195, doi:10.1126/science.1153 883.

Lindzen, R. S. and A. Y. Hou, 1988: Hadley circulations for zonally averaged heating centered off the equator. *J. Atmos. Sci.*, **45 (17)**, 2416–2427.

Lindzen, R. S. and S. Nigam, 1987: On the role of sea surface temperature gradients in forcing low-level winds and convergence in the tropics. *J. Atmos. Sci.*, **44**, 2418–2436.

Lu, J., G. Chen, and D. M. W. Frierson, 2008: Response of the zonal mean atmospheric circulation to El Niño versus global warming. *J. Climate*, **21**, 5835–5851.

Lu, J., G. A. Vecchi, and T. Reichler, 2007: Expansion of the Hadley cell under global warming. *Geophys. Res. Lett.*, **34**, L06 805, doi:10.1029/2006GL028 443.

Manabe, S., K. Bryan, and M. J. Spelman, 1975: A global ocean-atmosphere climate model. Part I: The atmospheric circulation. *J. Phys. Oceanogr.*, **5**, 3–29.

Mitas, C. M. and A. Clement, 2005: Has the Hadley cell been strengthening in recent decades? *Geophys. Res. Lett.*, **32**, L01 810, doi:10.1029/2005GL024 406.

Neale, R. B. and B. J. Hoskins, 2001a: A standard test for AGCMs including their physical parametrizations: I: The proposal. *Atmos. Sci. Lett.*, **1**, doi:10.1006/asle.2000.0019.

Neale, R. B. and B. J. Hoskins, 2001b: A standard test for AGCMs including their physical parametrizations: II: Results for the Met Office model. *Atmos. Sci. Lett.*, **1**, doi:10.1006/asle.2000.0020.

Neelin, J. and I. M. Held, 1987: Modeling tropical convergence based on the moist static energy budget. *Mon. Wea. Rev.*, **115**, 3–12.

Numaguti, A., 1993: Dynamics and energy balance of the hadley circulation and the tropical precipitation zones: Significance of the distribution of evaporation. *J. Atmos. Sci.*, **50 (13)**, 1874–1887.

Numaguti, A., 1995: Dynamics and energy balance of the Hadley circulation and the tropical

precipitation zones. Part II: Sensitivity to meridional SST distribution. *J. Atmos. Sci.*, **52 (8)**, 1128–1141.

Oort, A. and J. Yienger, 1996: Observed interannual variability in the Hadley circulation and its connection to ENSO. *J. Climate*, **9**, 2751–2767.

Pierrehumbert, R. T., 1995: Thermostats, radiators fins, and the local runaway greenhouse. *J. Atmos. Sci.*, **52**, 1784–1806.

Saravanan, R., 1993: Equatorial superrotation and maintenance of the general circulation in two-level models. *J. Atmos. Sci.*, **50**, 1211–1227.

Schneider, T., 2006: The general circulation of the atmosphere. *Ann. Rev. Earth Planet Sci.*, **34**, 655–688.

Seager, R., N. Harnik, Y. Kushnir, W. Robinson, and J. Miller, 2003: Mechanisms of hemispherically symmetric climate variability. *J. Climate*, **16**, 2960–2978.

Sobel, A. H., J. Nilsson, and L. M. Polvani, 2001: The weak temperature gradient approximation and balanced tropical moisture waves. *J. Atmos. Sci.*, **58**, 3650–3665.

Stone, P. H., 1978: Contrains on dynamical transports of energy on a spherical planet. *Dyn. Atmos. Oceans*, **2**, 123–139.

Suarez, M. J. and D. G. Duffy, 1992: Terrestrial superrotation: A bifurcation of the general circulation. *J. Atmos. Sci.*, **49**, 1541–1556.

Tanaka, H. L., N. Ishizki, and A. Kitoh, 2004: Trend and interannual variability of Walker,

monsoon and Hadley circulation defined by velocity potential in the upper troposphere. *Tellus A*, **56**, 250–269.

Trenberth, K. E. and D. P. Stepaniak, 2003: Seamless poleward atmospheric energy transports and implications for the Hadley circulation. *J. Climate*, **16**, 3706–3722.

Uppala, S. M., et al., 2005: The ERA-40 re-analysis. *Q. J. R. Meteorol. Soc.*, **131 (612)**, 2961–3012.

Vecchi, G. and B. Soden, 2007: Global warming and the weakening of the tropical circulation. *J. Climate*, **20**, 4316–4340.

Vecchi, G. A., B. J. Soden, A. T. Wittenberg, I. M. Held, A. Leetmaa, and M. J. Harrison, 2006: Weakening of the tropical atmospheric circulation due to anthropogenic forcing. *Nature*, **441**, 73–76.

Wang, B. and J. Chen, 1989: On the zonal-scale selection and vertical structure of equatorial intraseasonal waves. *Q. J. R. Meteorol. Soc.*, **115**, 1301–1323.

Williams, G. P., 2006: Circulation sensitivity to tropopause height. *J. Atmos. Sci.*, **63 (7)**, 1954–1961.

Williamson, D. L. and J. G. Olson, 2003: Dependence of aqua-planet simulations on time step. *Q. J. R. Meteorol. Soc.*, **129**, 2049–2064.

Yano, J.-I., W. W. Grabowski, and M. W. Moncrieff, 2002: Mean-state convective circulations over large-scale tropical SST gradients. *J. Atmos. Sci.*, **59**, 1578–1592.

Zhang, M. and H. Song, 2006: Evidence of deceleration of atmospheric vertical overturning circulation over the tropical Pacific. *Geophys. Res. Lett.*, **33**, L12 701, doi:10.1029/2006GL025 942.

List of Tables

1 Description of the SSTs used as lower boundary conditions in the aqua-planet simulations. The first set of experiments uses axisymmetric SST patterns to study the effects of the meridional SST gradients. The second set of simulations studies the effect of the zonal SST anomalies. The third set of simulations focuses on the response to a 2K uniform warming. ϕ designates the latitude. 44

2 Hadley and Walker circulations in the aqua-planet simulations. The differences between the control and +2K simulations, and between 0.5WAVE3 and WAVE3 are given. σ is the monthly standard deviation. The p-values of the student t-test test the differences of the means, the degree of freedom being calculated with the number of monthly outputs. $\max(\psi)$ and $\max(\psi_x^*)$ are respectively the maximum meridional streamfunction and zonal streamfunction anomalies, averaged between 700-hPa and 300-hPa. $\delta\chi_{200}$ and δSLP designate respectively the Walker circulation intensity described by the velocity potential at 200-hPa and SLP zonal gradients, averaged between 5°N and 5°S. 45

TABLE 1. Description of the SSTs used as lower boundary conditions in the aqua-planet simulations. The first set of experiments uses axisymmetric SST patterns to study the effects of the meridional SST gradients. The second set of simulations studies the effect of the zonal SST anomalies. The third set of simulations focuses on the response to a 2K uniform warming. ϕ designates the latitude.

Name of simulations	Name in Neale and Hoskins (2001a)	SST (°C)	Duration (months)
GRAD+2	PEAK	$27(1-\frac{3\phi}{\pi})$, $-\pi/3<\phi<\pi/3$ 0, if $\lvert\phi\rvert>\pi/3$	60
GRAD+1	CTRL	$27(1-\sin^2(\frac{3\phi}{2}))$, $-\pi/3<\phi<\pi/3$ 0, if $\lvert\phi\rvert>\pi/3$	60
REF	QOBS	mean between GRAD-1 and GRAD+1	60
GRAD-1	FLAT	$27(1-\sin^4(\frac{3\phi}{2}))$, $-\pi/3<\phi<\pi/3$ 0, if $\lvert\phi\rvert>\pi/3$	60
GRAD-2		$27(1-\sin^6(\frac{3\phi}{2}))$, $-\pi/3<\phi<\pi/3$ 0, if $\lvert\phi\rvert>\pi/3$	60
WAVE1		$\text{REF}+3\sin\lambda\cos^2\left(\frac{\pi}{2}\frac{\phi\pi}{9}\right)$ REF, if $\lvert\phi\rvert>2\pi/9$	168
WAVE2		$\text{REF}+3\sin 2\lambda\cos^2\left(\frac{\pi}{2}\frac{\phi\pi}{9}\right)$ REF, if $\lvert\phi\rvert>2\pi/9$	60
WAVE3		$\text{REF}+3\sin 3\lambda\cos^2\left(\frac{\pi}{2}\frac{\phi\pi}{9}\right)$ REF, if $\lvert\phi\rvert>2\pi/9$	168
0.5WAVE3		$\text{REF}+1.5\sin 3\lambda\cos^2\left(\frac{\pi}{2}\frac{\phi\pi}{9}\right)$ REF, if $\lvert\phi\rvert>2\pi/9$	60
REF+2K		REF + 2	60
WAVE1+2K		WAVE1 + 2, $-\pi/2<\phi<\pi/2$	168
WAVE2+2K		WAVE2 + 2, $-\pi/2<\phi<\pi/2$	60
WAVE3+2K		WAVE3 + 2, $-\pi/2<\phi<\pi/2$	60

TABLE 2. Hadley and Walker circulations in the aqua-planet simulations. The differences between the control and +2K simulations, and between 0.5WAVE3 and WAVE3 are given. σ is the monthly standard deviation. The p-values of the student t-test test the differences of the means, the degree of freedom being calculated with the number of monthly outputs. $\max(\psi)$ and $\max(\psi_x^*)$ are respectively the maximum meridional streamfunction and zonal streamfunction anomalies, averaged between 700-hPa and 300-hPa. $\delta\chi_{200}$ and δSLP designate respectively the Walker circulation intensity described by the velocity potential at 200-hPa and SLP zonal gradients, averaged between 5°N and 5°S.

Simulations	REF/ REF+2K	WAVE1/ WAVE1+2K	WAVE2/ WAVE2+2K	WAVE3/ WAVE3+2K	WAVE3/ 0.5WAVE3
$\max(\psi)$ $\pm\sigma$ (10^{10} kg s^{-1})	15.9 ± 0.8	7.7 ± 0.6	8.6 ± 0.8	10.7 ± 1.1	
$\Delta\psi$ (10^{10} kg s^{-1})	-0.6	+0.2	+0.1	+0.4	+0.9
$\Delta\psi/\psi$ (%)	-4.0%	+3.3%	+1.7%	+3.8%	+8.2%
p-value student t-test	0.00	0.02	0.23	0.00	0.00
$\max(\psi_x^*)$ $\pm\sigma$ (10^{10} kg s^{-1})	3.2 ± 0.8	9.8 ± 1.0	6.8 ± 0.8	4.2 ± 0.7	
$\Delta\psi_x^*$ (10^{10} kg s^{-1})	+0.3	+0.6	+0.3	-0.1	-0.4
$\Delta\psi_x^*/\psi_x^*$ (%)	+10.0%	+6.1%	+3.9%	-2.5%	-8.8%
p-value student t-test	0.01	0.00	0.05	0.21	0.00
$\delta\chi_{200}$ $\pm\sigma$ (10^6 m^2 s^{-1})	7.6 ± 0.2	13.7 ± 0.1	18.4 ± 0.1	21.2 ± 0.1	
$\Delta\chi_{200}$ (10^6 m^2 s^{-1})	+0.6	-0.2	-0.3	-0.6	-1.5
$\Delta\chi_{200}/\chi_{200}$ (%)	+6.1%	-2.3%	-3.5%	-0.6%	-15.0%
p-value student t-test	0.13	0.13	0.02	0.32	0.00
δSLP $\pm\sigma$ (Pa)	98 ± 31	718 ± 57	511 ± 38	439 ± 27	
$\Delta\delta SLP$ (Pa)	0	8	2	-8	-220
$\Delta\delta SLP/\delta SLP$ (%)	-0.0%	+1.2%	+0.3%	-2.0%	-50.0%
p-value student t-test	0.39	0.25	0.38	0.00	0.00

List of Figures

1 Sea Surface Temperature (°K) and zonal-mean precipitation (mm d^{-1}). (top left) SST and (top right) zonal-mean precipitation for the simulations where the meridional SST gradients are modified; (bottom left) SST anomalies in WAVE3 and (bottom right) zonal-mean precipitation in simulations with zonal SST anomalies. 51

2 Mean meridional streamfunction, in 10^{10} kg s^{-1} (contours), and zonal-mean zonal wind, in m s^{-1} (shades). 52

3 Hadley cell and jet stream characteristics. (top) Intensity and (bottom) latitudinal position in degree latitude of the Hadley cell and jet stream, for (left) simulations with different meridional SST gradients and (right) simulations with SST zonal anomalies. The latitudinal position of the jet streams is given by the location of the maximum zonal-mean zonal wind. The position of the subtropical and eddy-driven jets are given by the location of the maximum convergence flux of momentum by the zonal mean circulation and eddies (see Eqs. (3) and (4)). 53

4 Stationary eddy response to the zonal SST anomalies, for the simulation WAVE2. Left panel shows the geopotential anomalies in m (thin contours), the anomalous flow at the 200-hPa level, in m s^{-1} (vectors), and the zonal SST anomalies, in °K (thick contours). Right panel shows the zonal-mean stationary horizontal momentum transport in m^2 s^{-2}. 54

5 Geopotential anomalies in m (contours), the anomalous flow at the 200-hPa level, in m s^{-1} (vectors), and longitudinal SST anomalies in °K (thick contours) for the simulations (left) WAVE1 and (right) WAVE3. 55

6 Velocity potential at the 200-hPa height, χ_{200}, in 10^5 $m^2 s^{-1}$, in thin contours, for the simulation WAVE1 (upper-left panel), WAVE2 (upper-right) and WAVE3 (lower panels). The differences WAVE1+2K-WAVE1 (upper-left),WAVE2+2K-WAVE2 (upper-right), WAVE3+2K-WAVE3 (lower-left) and 0.5WAVE3-WAVE3 (lower-right) are shown in colors shades. The zonal SST anomalies are shown with thick contours. 56

7 Mean zonal streamfunction anomalies over the domain of the Hadley cells, in contours, for WAVE1 (top-left panel), WAVE2 (top-right) and WAVE3 (bottom left and right) simulations, in 10^{10} kg s^{-1}. The colors show the differences WAVE1+2K-WAVE1 (top-left panel), WAVE2+2K-WAVE2 (top-right), WAVE3+2K-WAVE3 (bottom-left) and 0.5WAVE3-WAVE3 (bottom-right). 57

8 Mean meridional streamfunction in contours, in 10^{10} kg s^{-1} in REF+2K (top-left panel), WAVE1+2K (top-right), WAVE3+2K (bottom-left) and WAVE3 (bottom-right). The colors show the differences REF+2K-REF(top-left panel), WAVE1+2K-WAVE1 (top-right), WAVE3+2K-WAVE3 (bottom-left) and 0.5WAVE3-WAVE3 (bottom-right). 58

9 Scatter plots illustrating the mean thermodynamic state of the tropical atmosphere. (upper panel) Column integrated water vapor, W, versus 500-hPa dry static stability, Sp_{500}. (middle panel) Dry static stability at 500-hPa versus mean ascending mid-tropospheric velocity, M^{+}_{500}. (lower panel) Precipitation, P, versus mean ascending mid-tropospheric velocity, M^{+}_{500}. All variables are averaged over the domain of the Hadley cells. 59

10 Zonal-mean zonal wind balance at the 200-hPa height, and contribution to the wind tendency in m s^{-1} day^{-1} from the mean advection, Coriolis torque, stationary and transient eddies. The continuous lines designate the results for the simulation REF, while the dashed lines indicate the results of the simulations GRAD-2 (top panel) and WAVE3 (bottom panel). 60

11 Zonal-mean MSE total flux, for the REF simulation, and decomposition into latent heat and DSE fluxes. The position of the Hadley cell, for REF, indicated by the latitude of the maximum (zero-value) meridional streamfunction, averaged between 300-hPa and 700-hPa, is shown with a thin (thick) black dashed vertical line. 61

12 Zonal-mean MSE flux, and decomposition into mean, transient and stationary components. The REF simulation is shown with dashed lines, while the GRAD+2 (top-left panel), GRAD-2 (top-right panel), WAVE3 (bottom-left panel) and REF+2K (bottom-right panel) are represented with continuous lines. The position of the Hadley cell, for REF, indicated by the latitude of the maximum (zero-value) meridional streamfunction, averaged between 300-hPa and 700-hPa, is shown with a thin (thick) black dashed vertical line. 62

13 Different terms of the zonal-mean MSE budget: L_vE, the turbulent latent heat flux, Q_R, the radiative cooling, H, the turbulent sensible heat flux and total, $Q_R + H + L_vE$. The REF simulation is shown with dashed lines, while the GRAD+2 (top-left panel), GRAD-2 (top-right panel), REF+2K (bottom-left panel) and WAVE2 (bottom-right panel) are represented with continuous lines. The position of the Hadley cell, for REF, indicated by the latitude of the maximum (zero-value) meridional streamfunction, averaged between 300-hPa and 700-hPa, is shown with a thin (thick) black dashed vertical line. 63

14 Deviation from the zonal-mean for the different terms of the meridional-mean MSE budget, averaged over the domain of the Hadley cells. L_vE is the turbulent latent heat flux, H, the turbulent sensible heat flux, Q_R, the radiative heating of the atmospheric column. Total designates the sum $Q_R + H + L_vE$. The continuous line illustrates the results for WAVE1+2K (upper panel), WAVE3+2K (middle panel) and 0.5WAVE3 (lower panel), while the dashed lines are for WAVE1 (upper panel) and WAVE3 (middle and lower panels). 64

15 Zonal-mean gross moist stability, in kJ kg^{-1}, in simulations using different meridional SST gradients (upper panel), uniform warming simulations (middle panel) and simulations with zonal SST anomalies (lower panel). 65

16 Intensity of the mean meridional circulation ψ, total MSE flux F, fraction of the MSE flux transported by the mean meridional circulation C and gross moist static stability Δm. The values are averaged over the deep tropics (between 2.5° and 15°). The errors bars show the monthly standard deviations. 66

17 Zonal streamfunction in the domain of the Hadley cells, for the ERA40 reanalysis in 10^{10} kg s^{-1}, for the period 1979-2001. (left panel) Zonal-mean zonal streamfunction $[\psi_x]$ and (right panel) zonal streamfunction anomalies ψ_x^*. 67

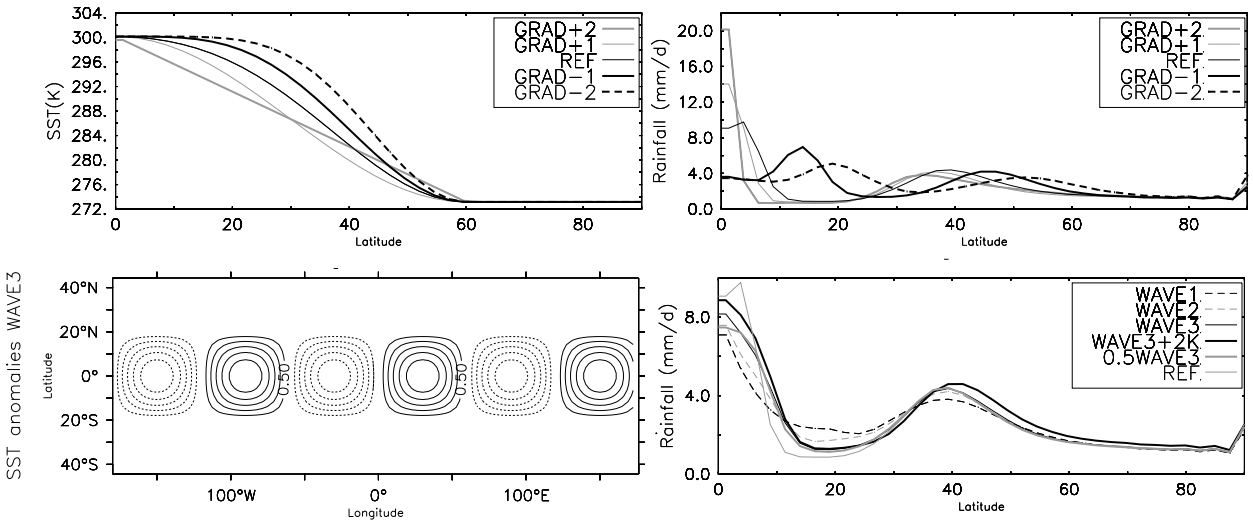

FIG. 1. Sea Surface Temperature (°K) and zonal-mean precipitation (mm d^{-1}). (top left) SST and (top right) zonal-mean precipitation for the simulations where the meridional SST gradients are modified; (bottom left) SST anomalies in WAVE3 and (bottom right) zonal-mean precipitation in simulations with zonal SST anomalies.

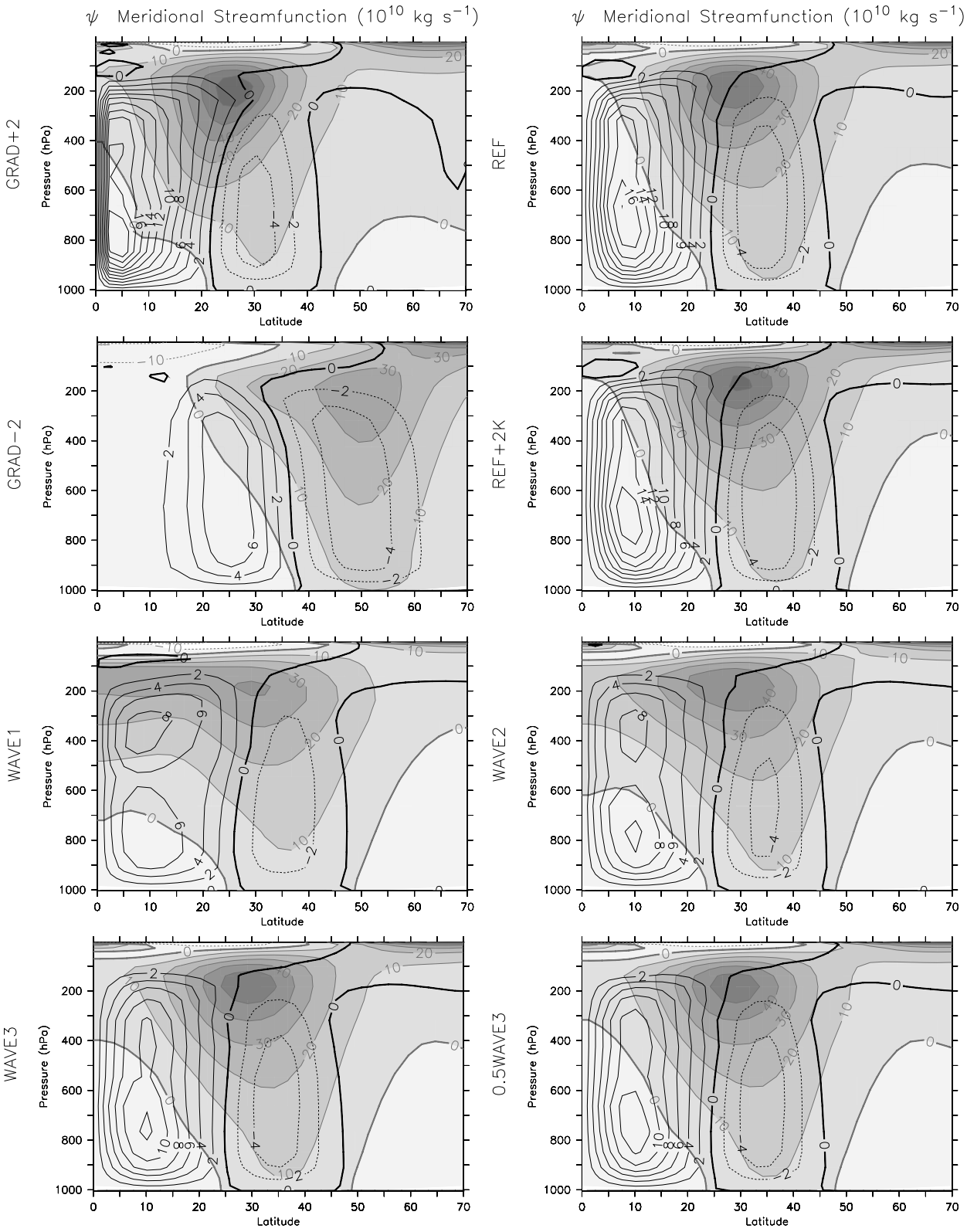

FIG. 2. Mean meridional streamfunction, in 10^{10} kg s^{-1} (contours), and zonal-mean zonal wind, in m s^{-1} (shades).

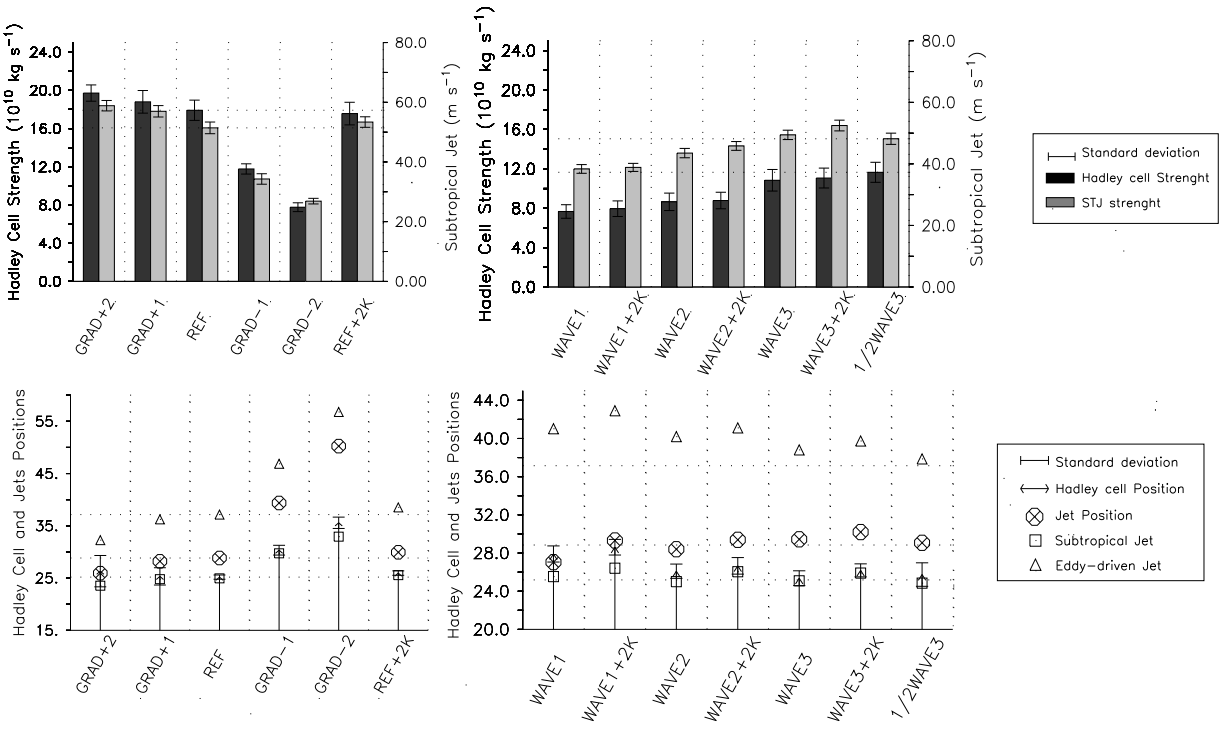

FIG. 3. Hadley cell and jet stream characteristics. (top) Intensity and (bottom) latitudinal position in degree latitude of the Hadley cell and jet stream, for (left) simulations with different meridional SST gradients and (right) simulations with SST zonal anomalies. The latitudinal position of the jet streams is given by the location of the maximum zonal-mean zonal wind. The position of the subtropical and eddy-driven jets are given by the location of the maximum convergence flux of momentum by the zonal mean circulation and eddies (see Eqs. (3) and (4)).

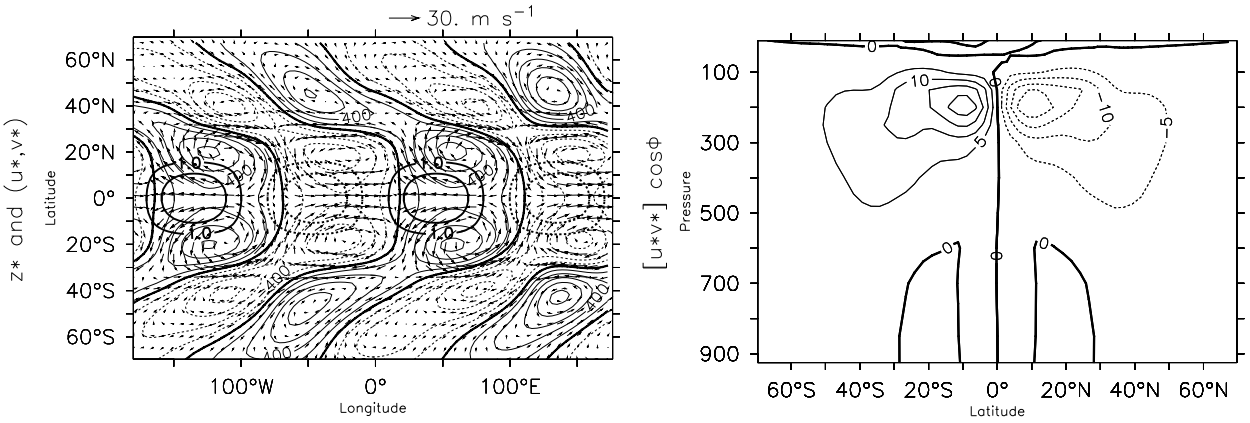

FIG. 4. Stationary eddy response to the zonal SST anomalies, for the simulation WAVE2. Left panel shows the geopotential anomalies in m (thin contours), the anomalous flow at the 200-hPa level, in m s^{-1} (vectors), and the zonal SST anomalies, in °K (thick contours). Right panel shows the zonal-mean stationary horizontal momentum transport in m^2 s^{-2}.

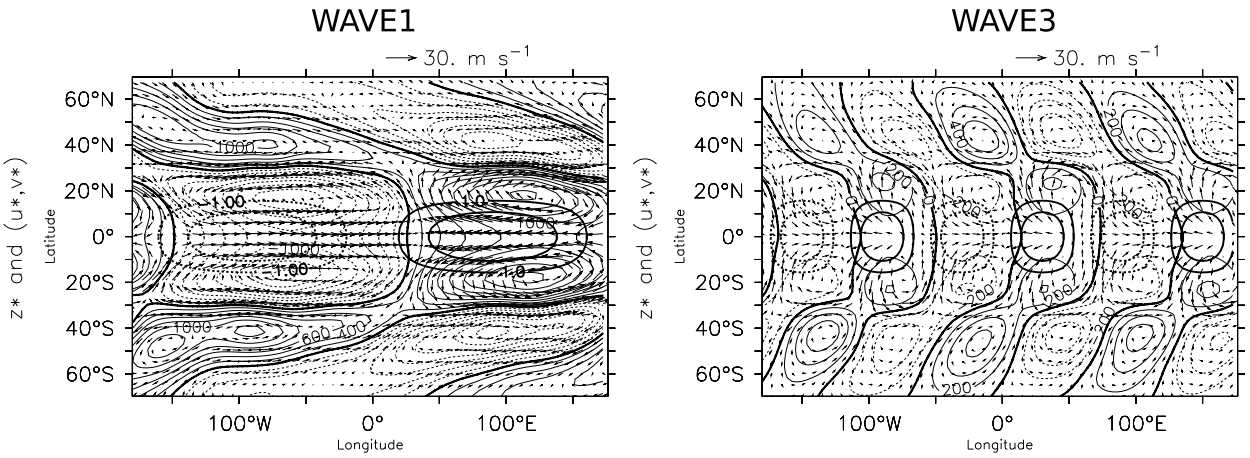

FIG. 5. Geopotential anomalies in m (contours), the anomalous flow at the 200-hPa level, in m s^{-1} (vectors), and longitudinal SST anomalies in °K (thick contours) for the simulations (left) WAVE1 and (right) WAVE3.

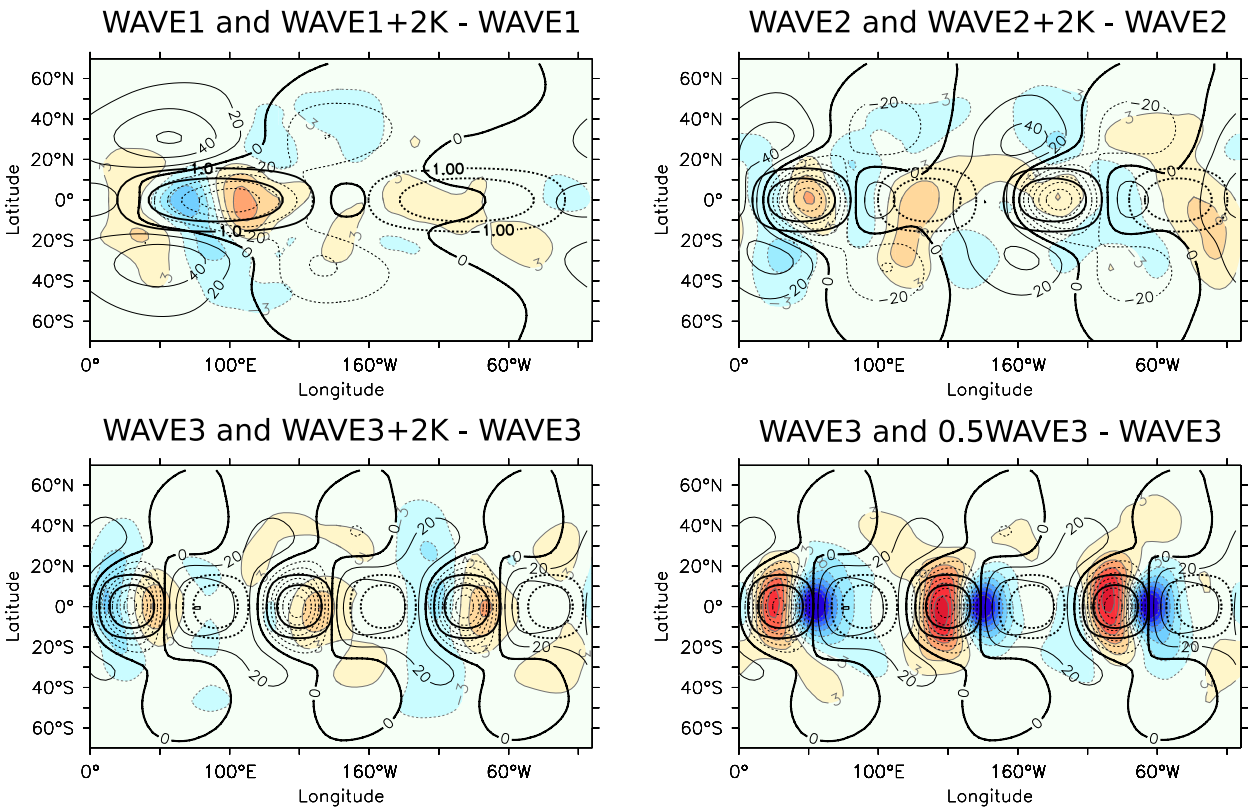

FIG. 6. Velocity potential at the 200-hPa height, χ_{200}, in 10^5 m^2s^{-1}, in thin contours, for the simulation WAVE1 (upper-left panel), WAVE2 (upper-right) and WAVE3 (lower panels). The differences WAVE1+2K-WAVE1 (upper-left),WAVE2+2K-WAVE2 (upper-right), WAVE3+2K-WAVE3 (lower-left) and 0.5WAVE3-WAVE3 (lower-right) are shown in colors shades. The zonal SST anomalies are shown with thick contours.

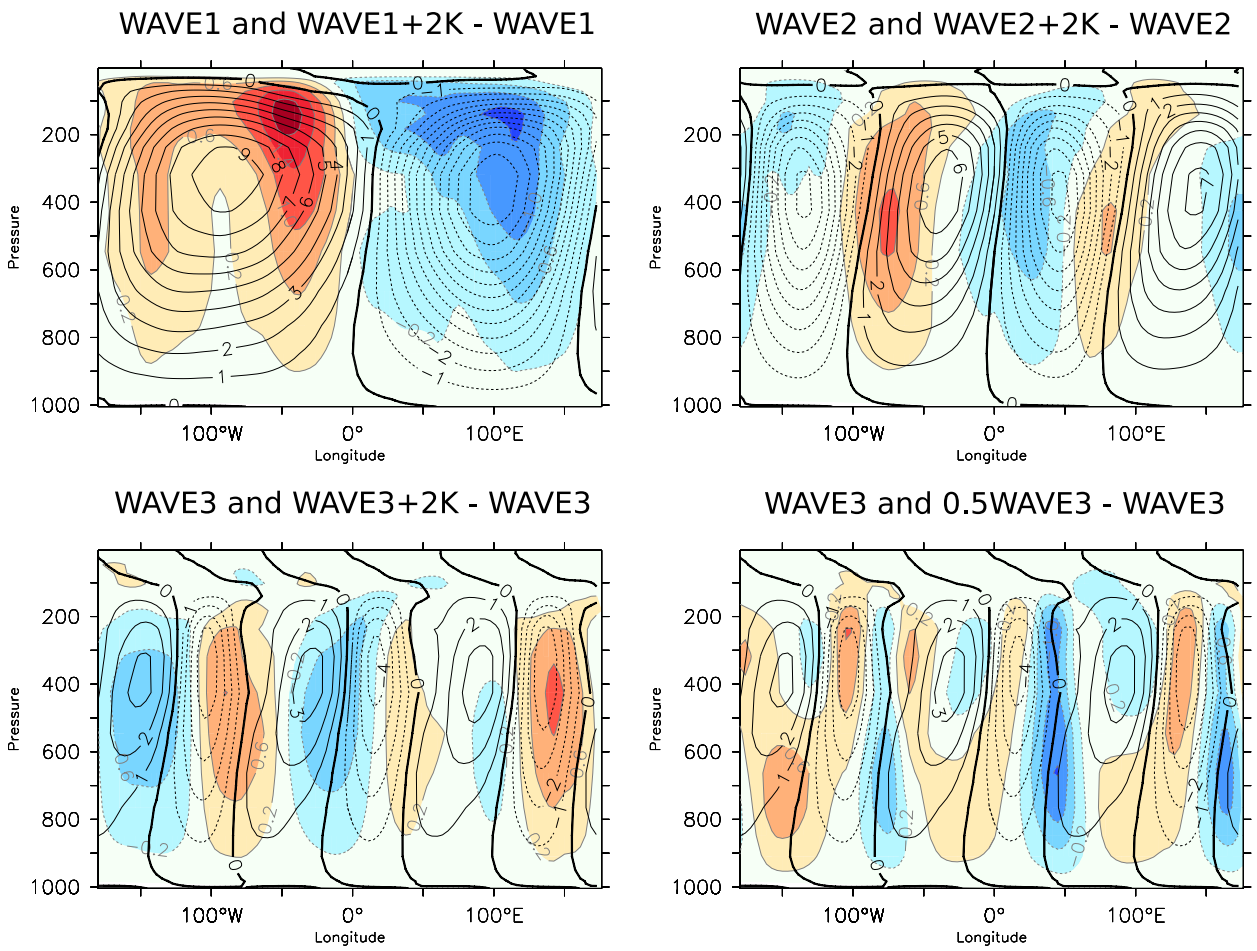

FIG. 7. Mean zonal streamfunction anomalies over the domain of the Hadley cells, in contours, for WAVE1 (top-left panel), WAVE2 (top-right) and WAVE3 (bottom left and right) simulations, in 10^{10} kg s^{-1}. The colors show the differences WAVE1+2K-WAVE1 (top-left panel), WAVE2+2K-WAVE2 (top-right), WAVE3+2K-WAVE3 (bottom-left) and 0.5WAVE3-WAVE3 (bottom-right).

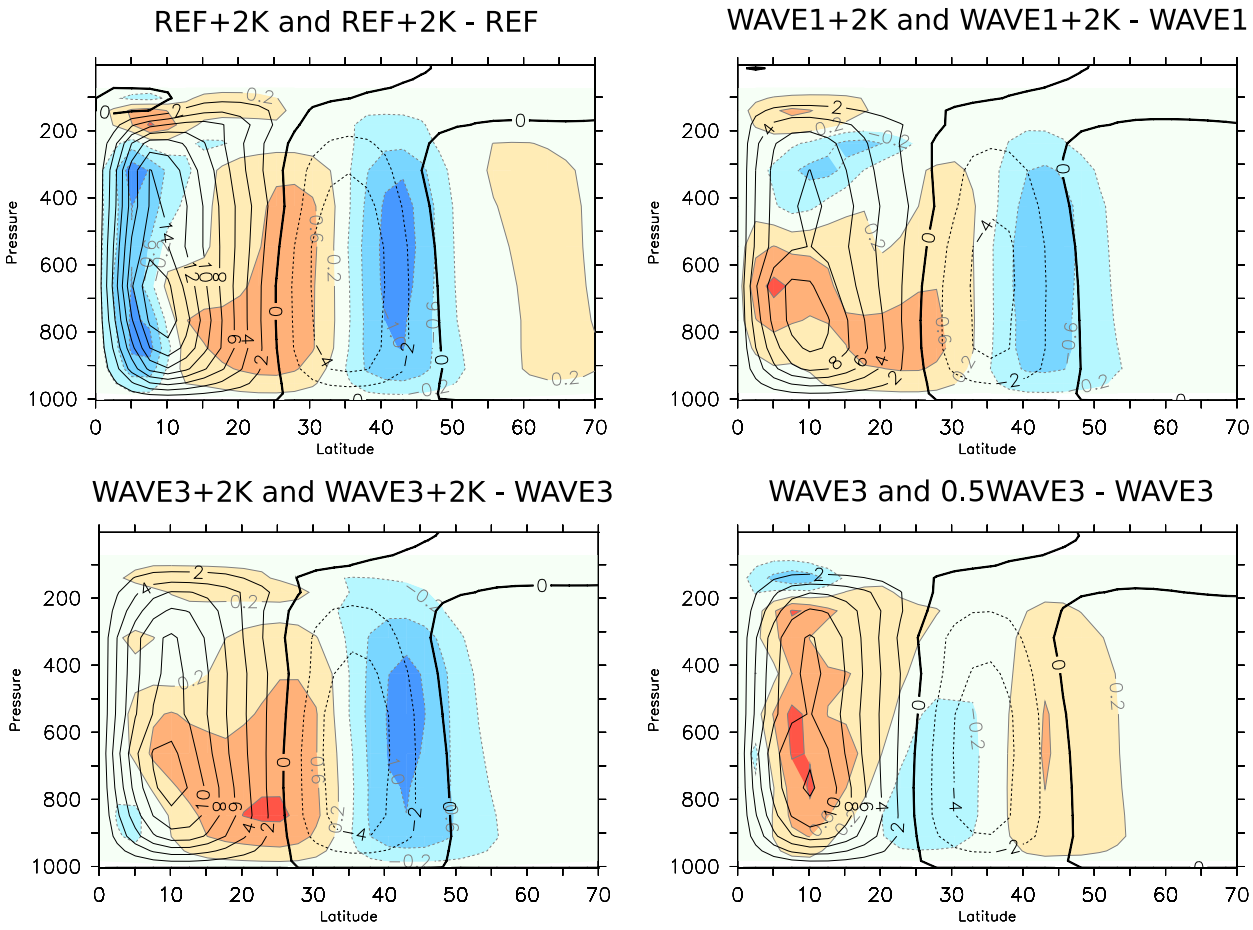

FIG. 8. Mean meridional streamfunction in contours, in 10^{10} kg s^{-1} in REF+2K (top-left panel), WAVE1+2K (top-right), WAVE3+2K (bottom-left) and WAVE3 (bottom-right). The colors show the differences REF+2K-REF(top-left panel), WAVE1+2K-WAVE1 (top-right), WAVE3+2K-WAVE3 (bottom-left) and 0.5WAVE3-WAVE3 (bottom-right).

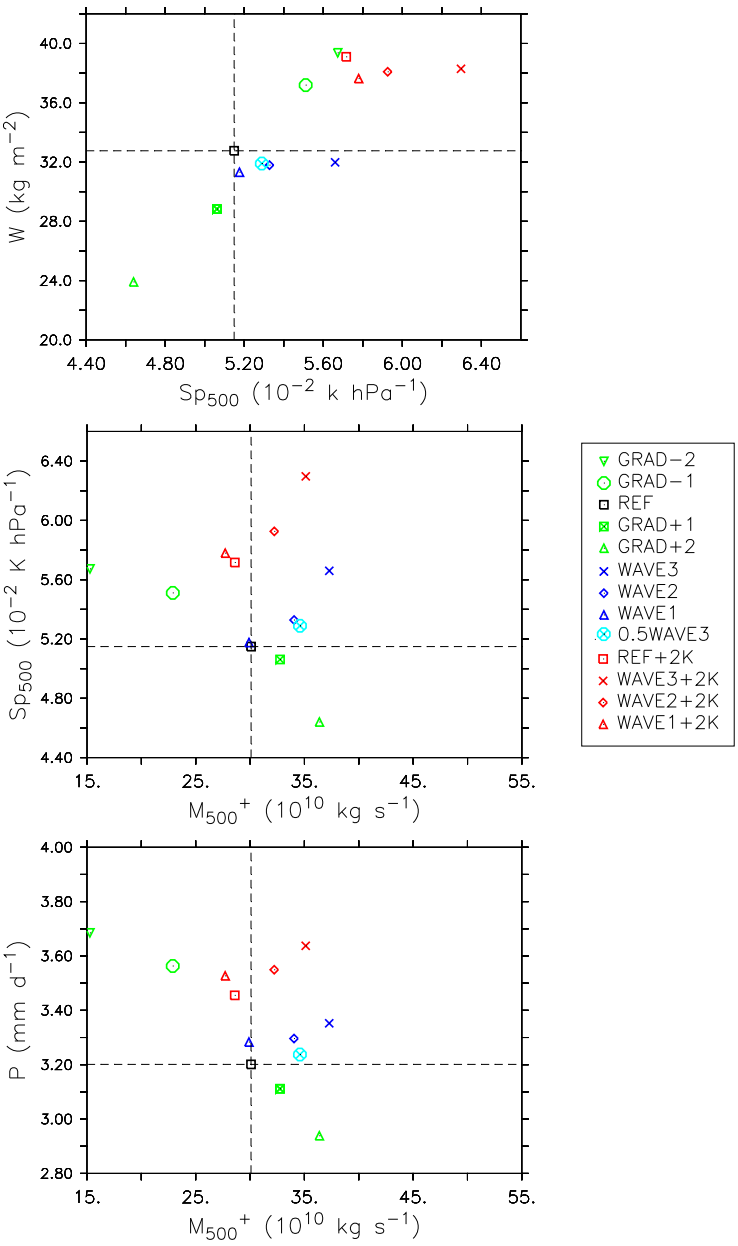

FIG. 9. Scatter plots illustrating the mean thermodynamic state of the tropical atmosphere. (upper panel) Column integrated water vapor, W, versus 500-hPa dry static stability, Sp_{500}. (middle panel) Dry static stability at 500-hPa versus mean ascending mid-tropospheric velocity, M_{500}^{+}. (lower panel) Precipitation, P, versus mean ascending mid-tropospheric velocity, M_{500}^{+}. All variables are averaged over the domain of the Hadley cells.

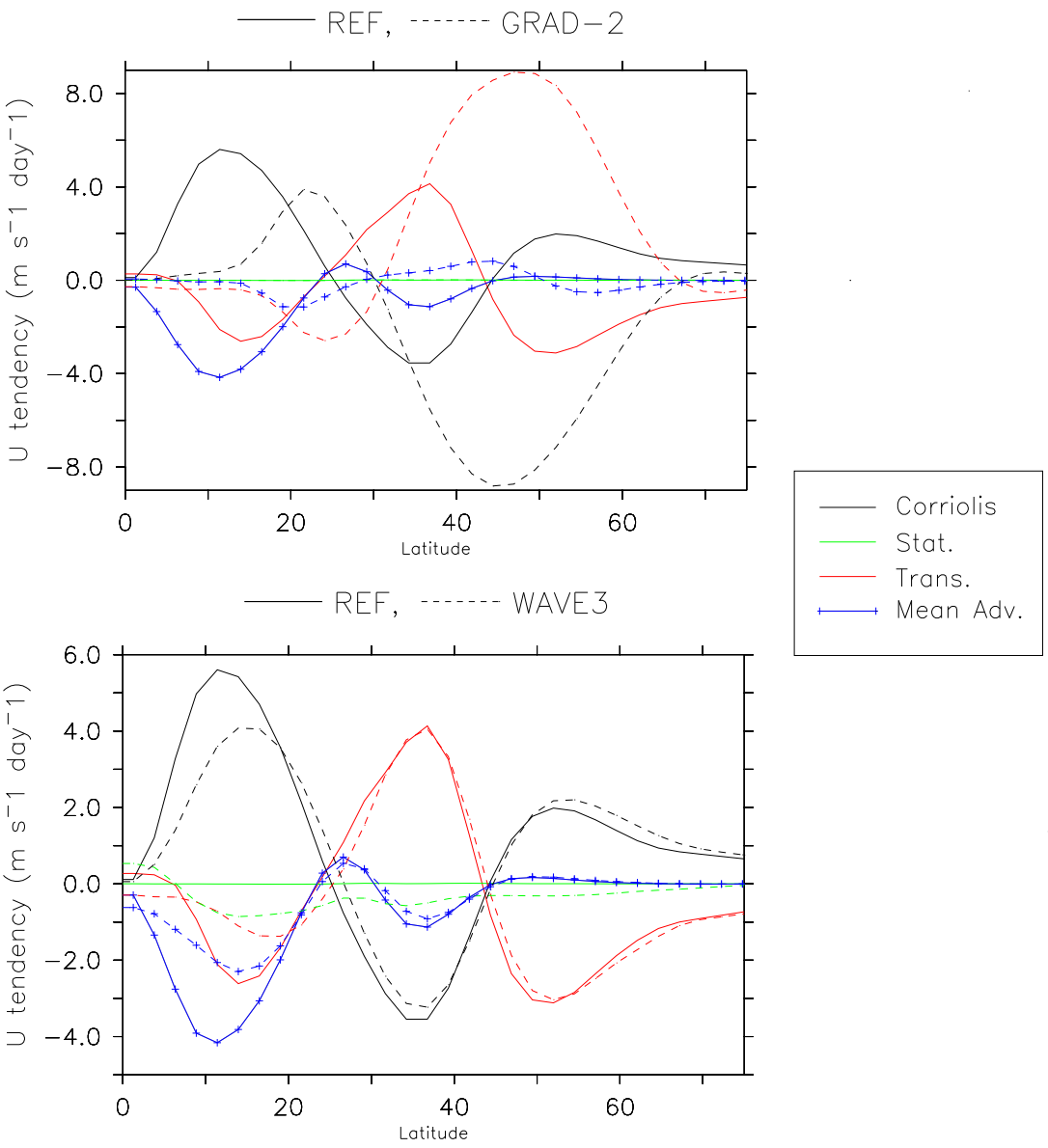

FIG. 10. Zonal-mean zonal wind balance at the 200-hPa height, and contribution to the wind tendency in m s^{-1} day^{-1} from the mean advection, Coriolis torque, stationary and transient eddies. The continuous lines designate the results for the simulation REF, while the dashed lines indicate the results of the simulations GRAD-2 (top panel) and WAVE3 (bottom panel).

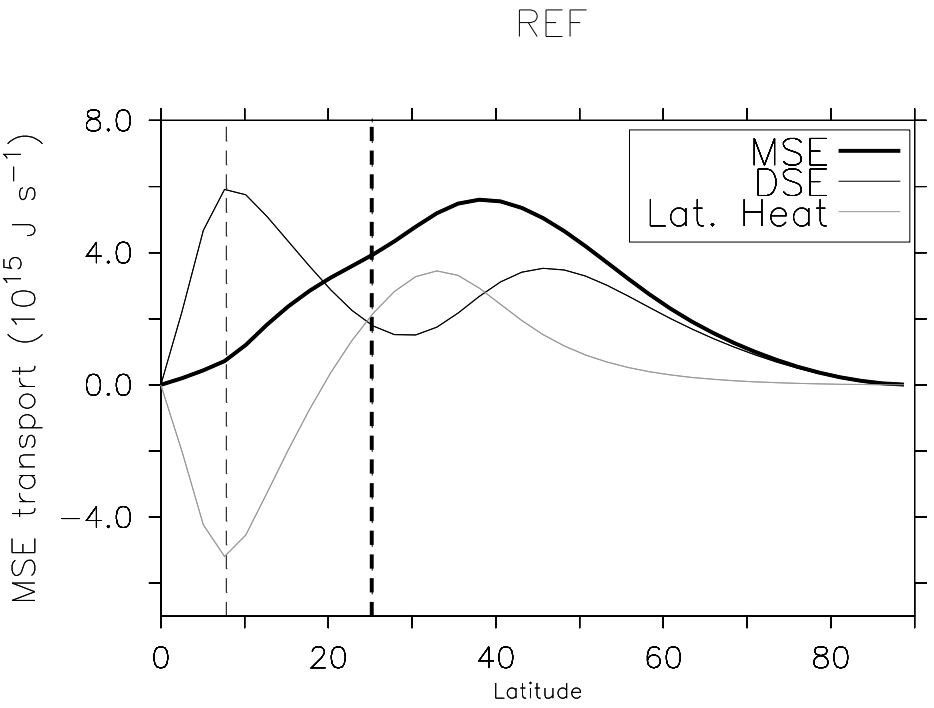

FIG. 11. Zonal-mean MSE total flux, for the REF simulation, and decomposition into latent heat and DSE fluxes. The position of the Hadley cell, for REF, indicated by the latitude of the maximum (zero-value) meridional streamfunction, averaged between 300-hPa and 700-hPa, is shown with a thin (thick) black dashed vertical line.

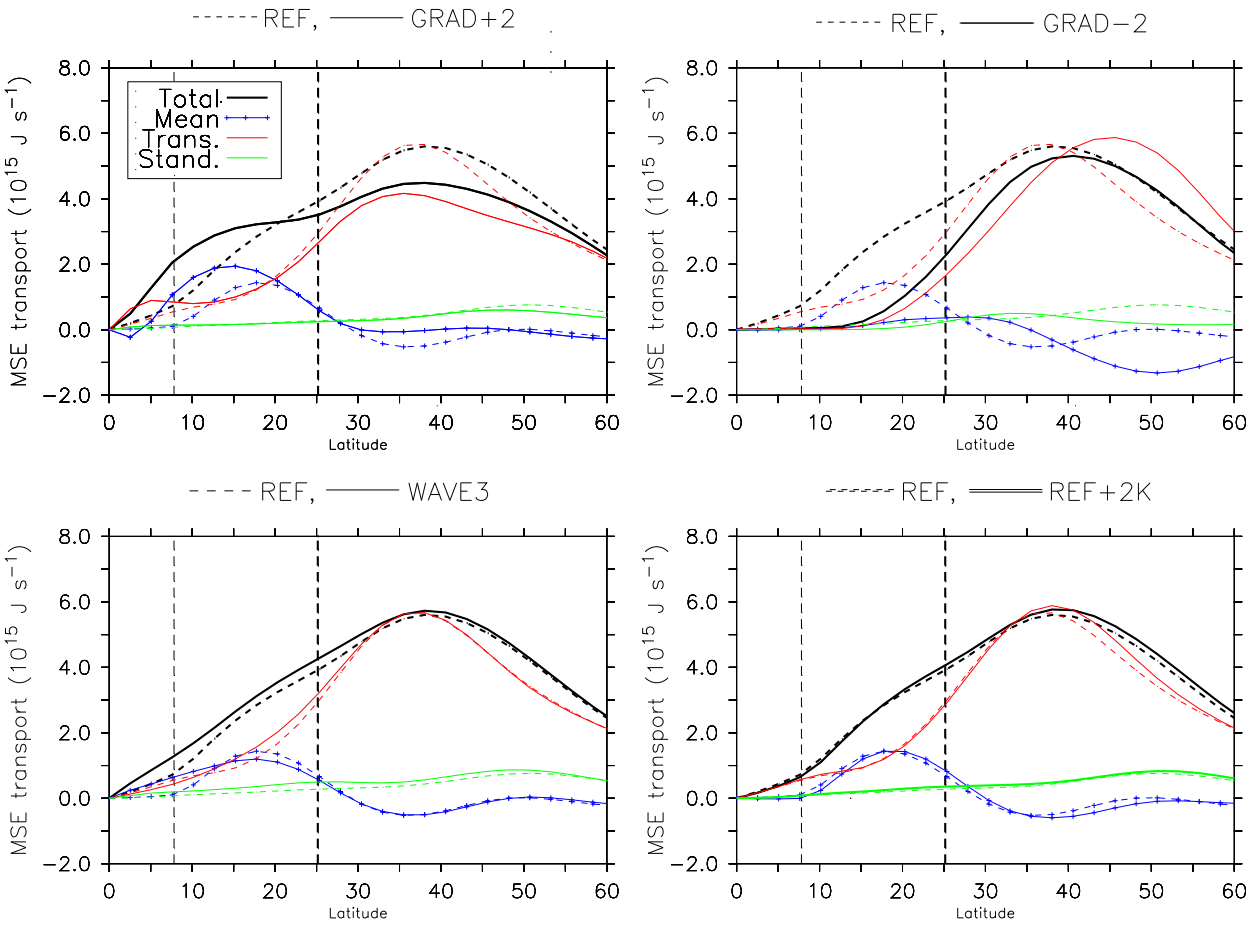

FIG. 12. Zonal-mean MSE flux, and decomposition into mean, transient and stationary components. The REF simulation is shown with dashed lines, while the GRAD+2 (top-left panel), GRAD-2 (top-right panel), WAVE3 (bottom-left panel) and REF+2K (bottom-right panel) are represented with continuous lines. The position of the Hadley cell, for REF, indicated by the latitude of the maximum (zero-value) meridional streamfunction, averaged between 300-hPa and 700-hPa, is shown with a thin (thick) black dashed vertical line.

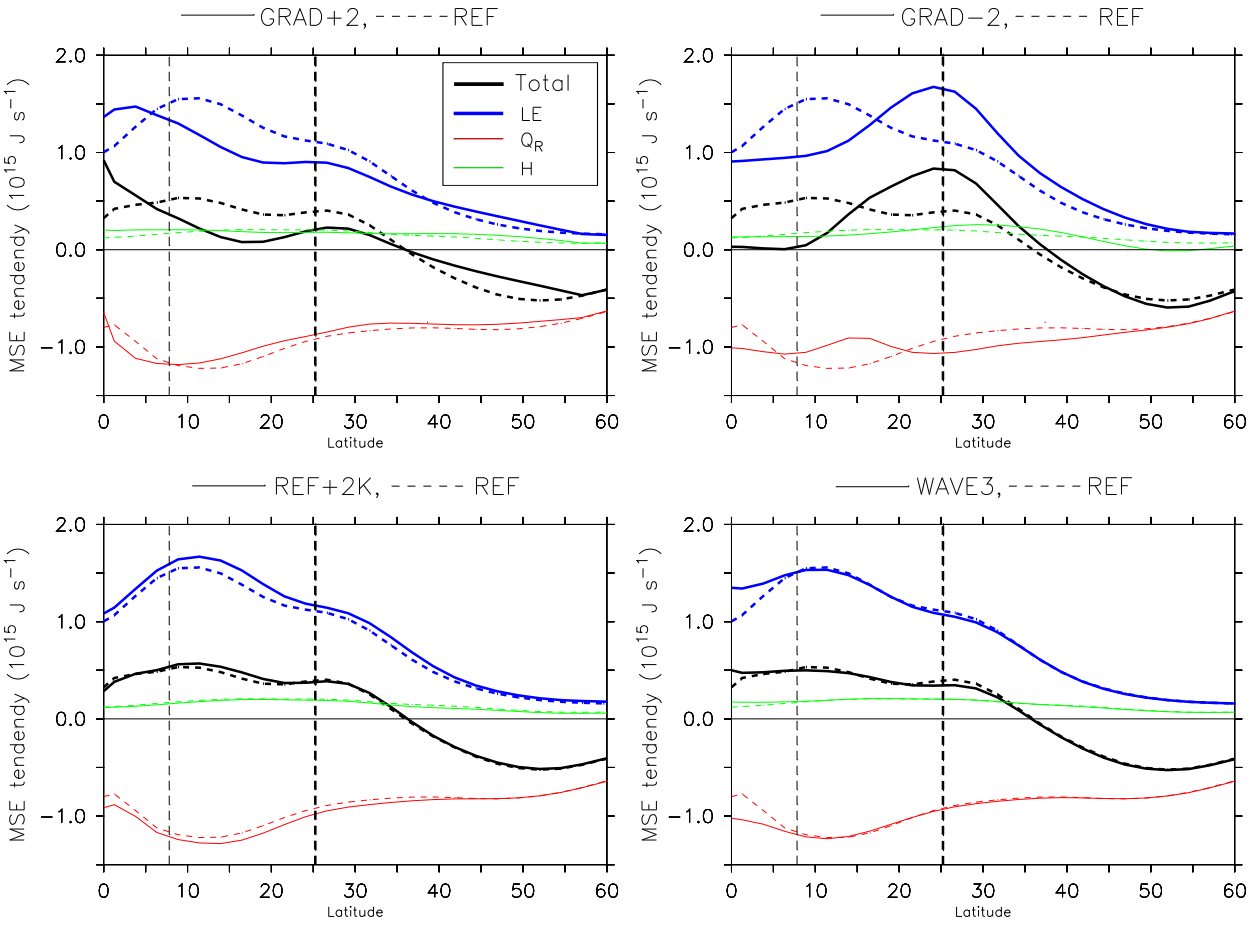

FIG. 13. Different terms of the zonal-mean MSE budget: L_vE, the turbulent latent heat flux, Q_R, the radiative cooling, H, the turbulent sensible heat flux and total, $Q_R + H + L_vE$. The REF simulation is shown with dashed lines, while the GRAD+2 (top-left panel), GRAD-2 (top-right panel), REF+2K (bottom-left panel) and WAVE2 (bottom-right panel) are represented with continuous lines. The position of the Hadley cell, for REF, indicated by the latitude of the maximum (zero-value) meridional streamfunction, averaged between 300-hPa and 700-hPa, is shown with a thin (thick) black dashed vertical line.

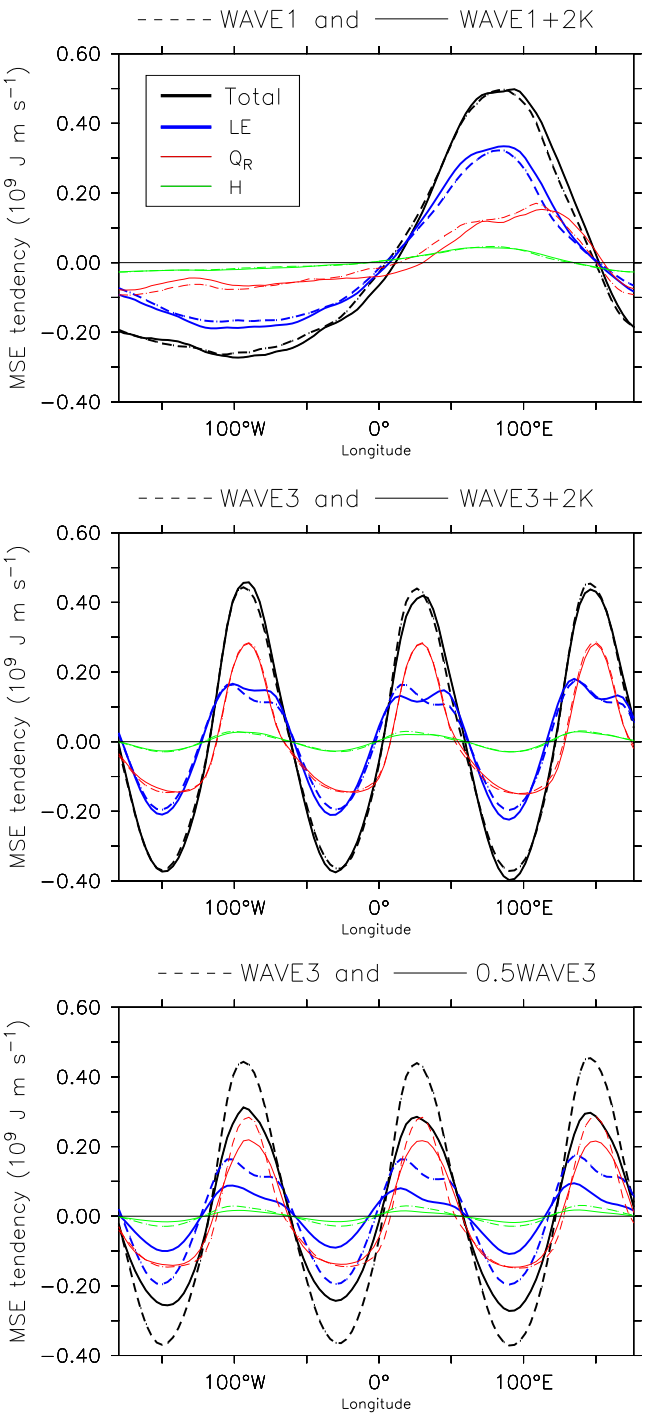

FIG. 14. Deviation from the zonal-mean for the different terms of the meridional-mean MSE budget, averaged over the domain of the Hadley cells. L_vE is the turbulent latent heat flux, H, the turbulent sensible heat flux, Q_R, the radiative heating of the atmospheric column. Total designates the sum $Q_R + H + L_vE$. The continuous line illustrates the results for WAVE1+2K (upper panel), WAVE3+2K (middle panel) and 0.5WAVE3 (lower panel), while the dashed lines are for WAVE1 (upper panel) and WAVE3 (middle and lower panels).

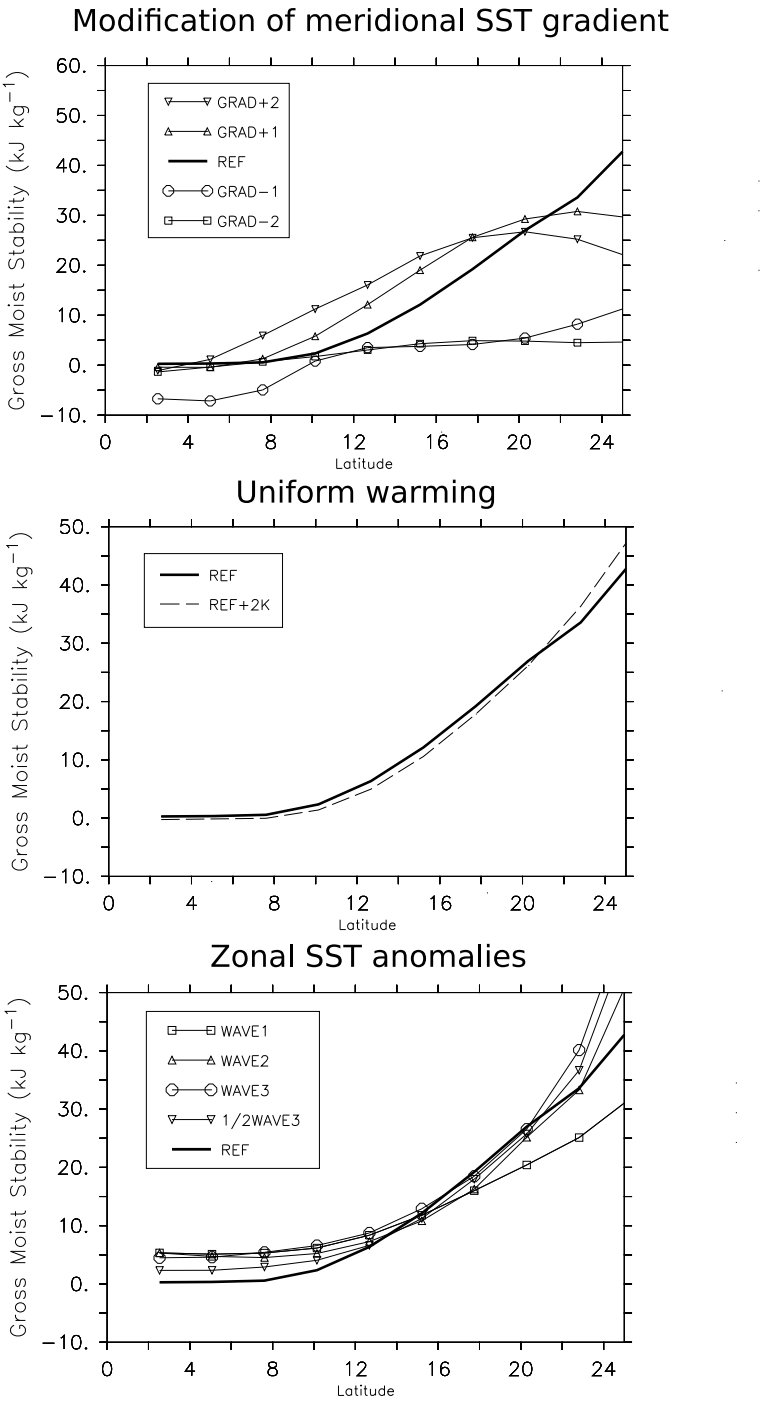

FIG. 15. Zonal-mean gross moist stability, in kJ kg^{-1}, in simulations using different meridional SST gradients (upper panel), uniform warming simulations (middle panel) and simulations with zonal SST anomalies (lower panel).

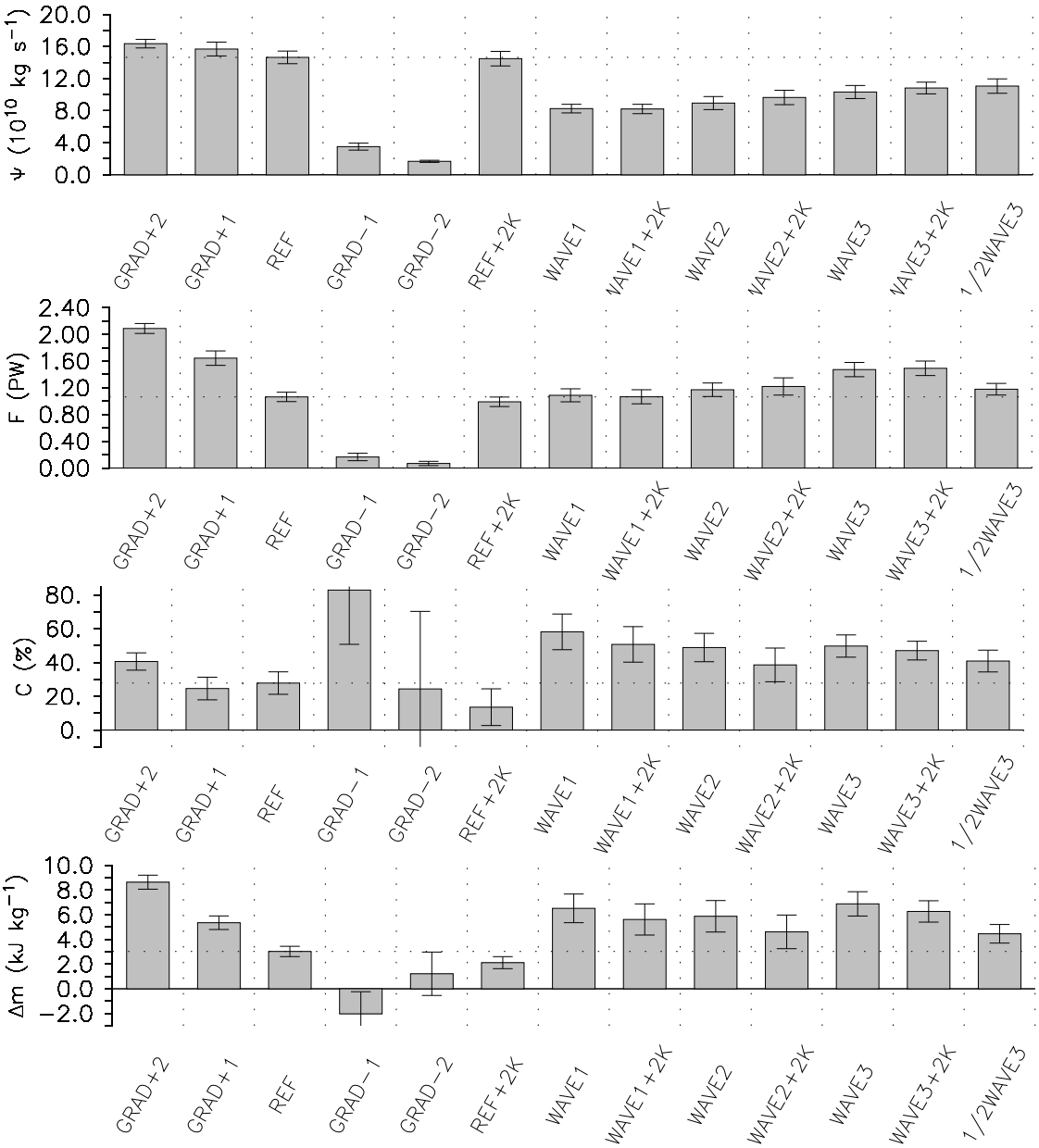

FIG. 16. Intensity of the mean meridional circulation ψ, total MSE flux F, fraction of the MSE flux transported by the mean meridional circulation C and gross moist static stability Δm. The values are averaged over the deep tropics (between 2.5° and 15°). The errors bars show the monthly standard deviations.

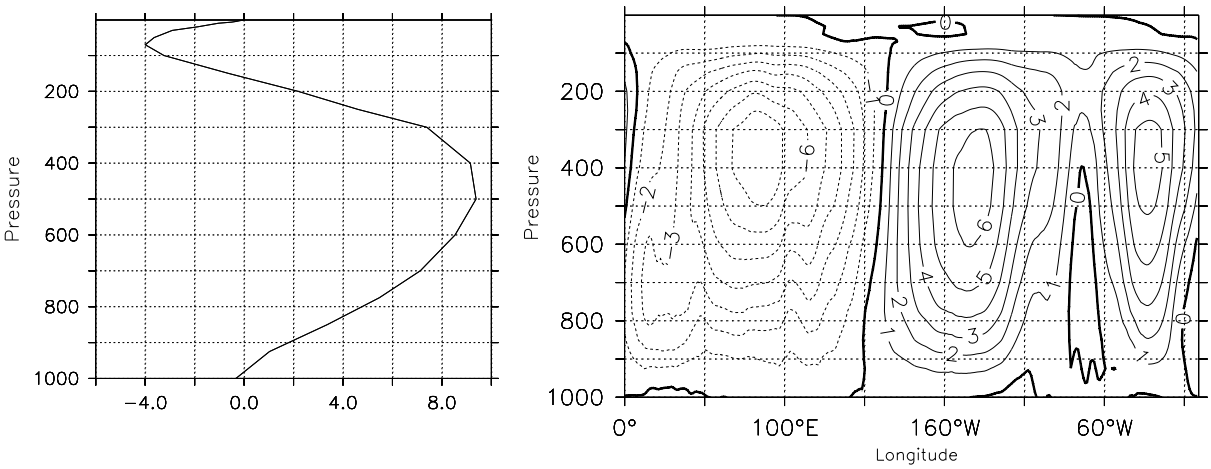

FIG. 17. Zonal streamfunction in the domain of the Hadley cells, for the ERA40 reanalysis in 10^{10} kg s^{-1}, for the period 1979-2001. (left panel) Zonal-mean zonal streamfunction $[\psi_x]$ and (right panel) zonal streamfunction anomalies ψ_x^*.